Review Responses for "A novel approach to characterize the variability in mass-Dimension relationships: results from MC3E"

We thank the reviewers for their careful reviews and constructive critique of our paper. We feel that responding to their comments has considerably improved the quality of the manuscript. In our response below, the comments of the reviewers are listed first, our response second, and changes to the text third. Page and line references in our response apply to a version of the revised manuscript that contains track changes and is included as a supplement, with added text wavy-underlined and in blue and discarded text struck out and in red.

Response to Comments of Reviewer 1:

Major comment #1: The methodology by which TWC and reflectivity (Z) are derived from the size distributions need to be explicitly stated, in equation form, at the first of the paper. TWC is never shown and Z is not shown until the discussion of how the equally plausible surfaces (EPS) are computed. It seems more logical to have the equations on TWC and Z prior to the error term rather than afterwards.

Response: An explanation of how TWC and Z was derived from the PSDs, including addition of Eq. (1) and Eq. (2) that define TWC_{SD} and Z_{SD}, has been added to line 27 on page 6.

Text: For an individual 10 s sample, the TWC and Z derived from the PSD for a specific a and b is given by TWC_{SD} and Z_{SD}, respectively, as

$$TWC_{\mathrm{SD}} = \sum_{j=1}^{N}(aD^b)N(D_j)dD_j \text{ and} \tag{1}$$

$$Z_{\mathrm{SD}} = \Big(\frac{6}{\pi\rho_{ice}}\Big)\frac{|K_{ice}|^2}{|K_w|^2}\sum_{j=1}^{N}(aD^b)^2N(D_j)dD_j \tag{2}$$

following the method of Hogan et al. (2006) and accounting for the different dielectric constants for water ($|K_w|^2 = 0.93$) and ice ($|K_{ice}|^2 = 0.17$). Uncertainties in the TWC_{SD} and Z_{SD} are discussed later in this section.

Major comment #2: When the computation of TWC and Z is introduced, there has to be a more vigorous discussion of the expected uncertainties when deriving the size and the mass from the 2D images. This is also why it becomes confusing at a later point when there is a discussion of the effective density and its impact on the EPS. What effective densities were used to derive TWC in the first place? Wouldn't that bound the uncertainty in the a&b coefficients?

Response: Potential uncertainties of TWC_{SD} and Z_{SD} are first acknowledged in line 25 on page 6, and are now numerically defined in the manuscript. Please see our response to Reviewer 2's major comment #5 for a full response and additions to the manuscript regarding measurement uncertainties from the OAPs, Nevzorov probe, and radar. As for how these uncertainties bound the a and b coefficients, this is now discussed in the manuscript on line 22 of page 8.

Major comment #3: How was the 10 second averaging period derived? Wouldn't it have been much more consistent to use variable sampling periods that always ensured statistically significant number of particles?

Response: Text has been added on page 4, line 13 to clarify that start and end times of each 10 s sampling periods were determined such that radar echo and microphysical data continuously existed throughout each 10 s period, thus ensuring that analysis did not include periods where the aircraft may be entering/exiting cloud. Further, points with the mean TWC for each 10 s period < 0.05 g m^{-3} were ignored (lines 17–18, page 4). Based on some of our previous work (e.g., McFarquhar et al., 2007 MWR), this suggests there are statistically significant numbers of particles for the analyzed time periods.

Text: Each 10 s period determined required radar echo and microphysical data for all 1 s samples to ensure that the aircraft and matched radar Z were completely in cloud during the 10 s period.

Text: Observations where the mean TWC for a 10 s interval < 0.05 g m^{-3} were ignored as the values were considered either below the noise threshold of the Nevzorov probe or optically thin cloud.

Major comment #4: What is the rational for equally weighting the TWC and Z error terms? To me, this is a significant assumption that needs a more thorough discussion. The Nevzorov TWC probe has a sample area much smaller than the 2D and HVPS while all three instruments sample a volume many orders of magnitude smaller than the radar. How do you reconcile these differences? If you construct the EPS from the TWC and Z independently, are they similar, or does TWC drive the minimization some of the time and the Z others? I understand, an appreciate, the care that was taken to obtain homogeneous samples from the Z data, but ask that my question be addressed in the manner I suggest.

Response: In general, we wanted the TWC and Z error terms to have approximately equal weight so that different portions of the measured size distribution would each be having some impact on the derived a/b coefficients (if we weighted according to the sample volume, this would be almost equivalent to not using any information from the bulk content probe). Discussion has been added to lines 12–21 on page 7 regarding how Z_{diff} was weighted using a priori assumptions of Z being proportional to the square of a particle's mass. Since cloud conditions often impact Z differently than TWC, TWC_{diff} has a greater impact on the χ^2 minimization technique some of the time and Z_{diff} has a greater impact on the minimization other times. Table 2 has been added to outline the relative difference between Z_{diff} and TWC_{diff} for each flight leg used in the study. TWC_{diff} and Z_{diff} were ultimately not adjusted to be given equal weight for each flight leg as that would have diminished the utility of using both TWC and Z observations, and limit the ability to diagnose periods when cloud properties influence TWC and Z differently.

Text: Given a priori assumptions of Z being proportional to the square of a particle's mass, the square root of reflectivity was used in Eq. (4) so that TWC_{diff} would be similar to Z_{diff} on average and each would have approximately equal weight in determining a and b. Although radar Z measurements involve a significantly greater sample volume than that of OAPs and a bulk content probe, TWC_{diff} and Z_{diff} were not weighted proportionally to the sample volume in order to ensure that both bulk moments had some impact on the derived a and b. Given that larger ice crystals are fractionally more important than small crystals in determining Z_{SD} than TWC_{SD} and given varying contributions of larger crystals to Z_{SD} and TWC_{SD}, TWC_{diff} has a greater impact on the χ^2 minimization procedure some of the time while Z_{diff} does at other times. The ratios between Z_{diff} and TWC_{diff} for each flight leg are given in Table 2, and range between 0.32 and 8.58 with a mean of 2.62 among the 16 flight legs. No attempt is made to force equal weight for Z_{diff} and TWC_{diff} for each coincident point because there are periods when cloud properties influence TWC differently than Z.

Major comment #5: I found the summary somewhat incomplete in that it concludes that there will always be a broad region of EPS in any given situation. If I am a radar or satellite scientist, this would lead me to throw up my hands, put the EPS chart on the door, and throw a dart. Is this what the authors suggest we do? If not, then I strongly suggest that the paper end on a more positive note that can recommend to the remote sensing community what should be done.

Response: Discussion has been added on line 28 of page 17 that emphasizes how the sizes of the EPS are related to the correlation between a and b and that the large variability in (a,b) does not necessarily relate to large uncertainties in all derived quantities. Suggestion of future work aimed at assessing the drivers behind the size of the EPS and also how the EPS can be applied within numerical models and remote sensing retrievals has also been added to the text.

Text: The results presented here illustrate that similar TWC and Z can be obtained regardless of the a and b values chosen, with coefficients randomly selected from a surface of solutions allowing one to represent how the uncertainty in (a,b) impacts any derived quantity. Thus, the large variability in derived (a,b) for an equally plausible surface does not necessarily indicate there is a large uncertainty in quantities derived using the a and b coefficients. Future work should assess how the representation of modeled processes and retrieved quantities are influenced by the variability in a and b coefficients as well as which environmental drivers and cloud microphysical properties influence the size of derived surfaces of equally plausible solutions, and the extent to which measurement errors need to be reduced to better refine these surfaces.

Minor comment #1: Why was the CIP not used? It is introduced as one of the probes on the aircraft, it has twice the number of diodes as the 2D-C, 100 mm between arms rather than 63, and hence more sample volume, yet it isn't used. Why?

Response: Text has been added to lines 16–25 on page 5 acknowledging the greater sample volume of the CIP, and an explanation of why the 2D-C having anti-shattering tips and very little indication of shattered artifacts from inter-arrival time distributions provided an advantage over the CIP for this particular study as explained in Wu and McFarquhar (2016). Closer examination of that manuscript and of the size distribution code used to produce the PSDs prompted removing text on page 5, line 21 of the original manuscript that mentioned use of an inter-arrival time threshold for the 2D-C.

Text: The 2D-C was used instead of the CIP in the analysis even though the CIP has a larger sample volume because the inclusion of anti-shattering tips on the 2D-C reduced the impact of shattered artifacts (e.g., Korolev et al., 2011). Previous studies (Korolev et al., 2011, 2013a; Jackson et al., 2014) have shown that use of algorithms to identify shattered artifacts are sometimes needed even when the OAP is equipped with anti-shattering tips. Artifacts are identified by examining the frequency distribution of the times between which particles enter the sample volume (inter-arrival time; Field et al., 2006). When artifacts are present, this distribution follows a bimodal distribution with naturally-occurring particles having a mode with longer inter-arrival times and shattered artifacts having a mode with shorter inter-arrival times (e.g., Field et al., 2003). During MC3E there was only one mode in the inter-arrival time distribution corresponding to the naturally-occurring particles (Wu and McFarquhar, 2016) at all times, suggesting there were few shattered artifacts. Therefore, no shattering removal algorithm was used for the 2D-C and HVPS.

Minor comment #2: How are the 2D-C and HVPS size distributions combined? Do they always overlap well? If not, how is this reconciled?

Response: While some studies have used variable weighting within the overlap region to produce a smoother transition in *N(D)* between two OAPs (e.g., Fontaine et al., 2014 ACP), the small discrepancy in *N(D)* within the overlap region (5%) characterized for the MC3E campaign justified use of a single, consistent cutoff of 1 mm for Wu and McFarquhar (2016) and this study. Text has been added on line 26 of page 5 to clarify this point.

Text: The 1 mm cutoff was chosen since *N(D)* for the two OAPs agreed on average within 5 percent for $0.8 \leq D \leq 1.2$ mm, and was used for all PSDs irrespective of periods when the difference between *N(D)* for the OAPs exceeded 5% in the overlap region.

Minor comment #3: Error analysis, error analysis, error analysis. What are the expected uncertainties in the EPS due to choice of size and effective density?

Response: The derived EPS now account for uncertainties due to measurement error from the OAPs, Nevzorov *TWC* probe, and the radar reflectivity. Please see our response to Reviewer 2's major comment #5 for a full response addressing these measurement errors.

Minor comment #4: Page 5, line 17. Following Heymsfield and Baumgardner (1985) and Field (1999), only particles with a center of mass within the OAP's field of view were considered as otherwise there is too much uncertainty in particle shape.. Several corrections/questions here. First of all, it it the center of mass being located in the field of view or center of the measured image? In either case, how is this determined? Finally, using the center-in technique mostly reduces uncertainty in size, not in shape.

Response: The text on lines 1–8 of page 6 have been modified to clarify the points above, and to briefly describe the criterion used to determine whether a particle was center-in.

Text: Following Heymsfield and Baumgardner (1985) and Field (1999), only particles imaged with their center within the OAP's field of view were considered as otherwise there is too much uncertainty in particle size. Particles were identified as having their center within the field of view if their maximum dimension along the time direction exceeded the largest length where the particle potentially touched the edge of the photodiode array.

Minor comment #5: Equation 3 shows TWC being averaged not Z, but don't the derived Zs also get averaged?

Response: The reviewer is correct in that reflectivity is also averaged in the χ^2 calculation. This was properly computed for the study, and a pair of brackets has been placed around the TWC_{diff}(i) + Z_{diff}(i) term of Eq. (3) (now Eq. (5) in the revised manuscript) to clarify this calculation.

Response to Comments of Reviewer 2:

Major comment #1: Manuscript needs to document equation illustrating how Z is calculated from PSD.

Response: An explanation of how TWC and Z were derived from the PSDs, including addition of Eq. (1) and Eq. (2) that define TWC_{SD} and Z_{SD}, has been added on line 27 of page 6. Please see the response to Reviewer 1's major comment #1 for a full description.

Major comment #2: The authors have to quantify and discuss S band radar reflectivity factor sensitivity as a function of crystal size.

Response: The addition of how Z is computed from particle size distributions (Eq. (2) in the revised manuscript) should show that smaller particles do not make as large of contributions to radar reflectivity at S-band as do larger particles given the dependence of radar reflectivity on mass-squared. Further, an example of the cumulative reflectivity distribution function (Fig. (4)) reiterates the point that small particles make small contributions to Z (note the y-axis is on a log-scale in the figure).

Major comment #3: Don't use B&F for MMD$_{max}$ calculation (Fig 11, etc... and respective arguments in text). B&F has been retrieved for mean chord length size definition and therefore would necessarily overestimate TWC, real MMD_{max}, etc...when using PSD in D_{max} definition.

Response: The Brown and Francis (BF95) coefficients mentioned in the manuscript were the modified values of Hogan et al. (2012) that correspond to the same definition of particle maximum dimension used in this study. While any set of m-D coefficients from previous studies could have been used for comparison purposes, the BF95 coefficients were chosen because they are well cited in the literature. These points have been clarified in lines 28–29 on page 9 (first excerpt below) and lines 14–15 on page 13 (second excerpt below), and text mentioning the BF95 coefficients were modified throughout the remainder of the manuscript to emphasize the modified coefficients were applied in the calculations.

Text: The $Z_c(D)$ derived using BF95 coefficients, with the prefactor a (=0.002 g $\mathrm{cm}^{-1.9}$) modified following the correction factor of Hogan et al. (2012) applicable for the definition of D used here, is also shown for reference. It is worth noting that the modified BF95 coefficients may reasonably resolve the particle mass for some particle sizes for the PSD depicted in Fig. 4.

Text: The D_{mm} is derived using the modified BF95 coefficients to compare among the different flight legs.

Major comment #4: Either the manuscript has to derive mathematically how TWC_{diff} (equ 1) and Z_{diff} (equ. 2) can be merged into a sum or likewise into chi-square (equ.3) both to be minimized subsequently (Fig 2). As it stands, we feel that differences (measured, calculated from PSD) of the square root of Z may be a bit comparable to respective differences in TWC, in order to merge those two terms. Of course this is scientifically insufficient... The authors may think about sensitivity studies for table 1 data to know which term controls chi-square (equ 3), as a function of different flight legs and how this evolves during individual flight legs.

Response: The relative importance of different particle sizes to calculations of bulk parameters is different for Z and TWC (Z is more sensitive to larger particles than is TWC). Thus, depending on the relative concentrations of different sized particles, Z and TWC will be impacted differently depending on the cloud conditions and size distributions present. For the analysis presented in the manuscript, TWC_{diff} has a greater impact on the χ^2 minimization technique some of the time and Z_{diff} some other times. Table 2 has been added to outline the magnitude of Z_{diff} and TWC_{diff} for each flight leg used in the study. TWC_{diff} and Z_{diff} were ultimately not adjusted to be given equal weight in determining the (a,b) coefficients for each flight leg as doing so would diminish the utility of using both TWC and Z observations, and limit the ability to diagnose periods when varying size distributions influence TWC and Z differently. Please see the response to Reviewer 1's major comment #4 for further details and how this point has been addressed in the text.

Major comment #5: Poisson statistics doesn't take into account systematic uncertainties in measuring TWC from Nevzorov and not systematic errors in Z measurements. Within a homogeneous cloud segment the statistical counting uncertainty is small, but systematic measurement uncertainty can be of the order of 50% or 100 %... This has to be taken into account instead of Poisson statistics that seems serving to get rid of the uncertainty discussion... ? To resume, the tolerance of EPS has to take into account real uncertainties and not just Poisson statistics / natural variability.

Response: The reviewer makes a good point here. The chi-square minimization procedure has been modified to consider measurement uncertainties from the OAPs, Nevzorov probe, and radar. As a result, figures related to the equally plausible surfaces are different for some of the flight legs than those present in the original manuscript. The allowable tolerance $\Delta\chi^2$ for a flight leg now considers the maximum value of the following quantities: natural variability (χ^2_{min}), uncertainty due to Poisson statistics ($\Delta\chi^2_1$), and measurement uncertainties ($\Delta\chi^2_2$). This last term is outlined in Eq. (7) and described on line 22 of page 8. It considers a 50% uncertainty in the PSDs when deriving TWC_{SD} and Z_{SD} (see Heymsfield et al. [2013] and related text in this manuscript), a 2–8% uncertainty in the Nevzorov TWC measurements (see Korolev et al. [2012] and related text in this manuscript), and a 1 dBZ uncertainty in the radar Z measurements (see Krajewski and Ciach [2003] and related text in this manuscript). Fig. 3 has been modified to include distributions of the ratio between χ^2_{min} and $\Delta\chi^2_2$, and key finding #4 in the conclusions section has been modified accordingly.

Text: Estimates of the measurement uncertainty from the OAPs, Nevzorov probe, and ground-based radar also influence the uncertainty in the derived coefficients. The uncertainty due to measurement error $\Delta\chi^2_2$ is defined as [the sum of measurement error from the OAPs, Nevzorov TWC probe, and radar]. The terms $TWC_{SD,meas\_min}$, $TWC_{SD,meas\_max}$, $Z_{SD,meas\_min}$, and $Z_{SD,meas\_max}$ represent the minimum and maximum TWC or Z derived using a 50% uncertainty in the measured *N(D)*. This uncertainty follows Heymsfield et al. (2013) where up to a 50% difference in the number concentration for particles with D $>$ 0.1 mm was determined. Uncertainties in the bulk measurements of TWC and Z must also be considered in the generation of the uncertainty surfaces with the minimum and maximum possible bulk values represented as TWC_{meas_min}, TWC_{meas_max}, Z_{meas_min}, and Z_{meas_max}. Following Korolev et al. (2013b), it was assumed that there was a 2% uncertainty when Dmax $\leq$ 4 mm and a 8% uncertainty for other periods to address the possibility of particles bouncing out of the cone of the Nevzorov probe. A radar reflectivity uncertainty of 1 dB (Krajewski and Ciach, 2003) is subtracted from or added to the measured Z to determine Z_{meas_min} and Z_{meas_max}.

Major comment #6: Recommendation to limit b to 1-3. As a consequence delete everything from pg 7 line 20 to pg 8 line 21, since this discussion finally does not contribute to the study. I don't see the physical meaning to go beyond b=3 of a sphere, mathematically of course one may not care about an interpretation.

Response: Although equally plausible solutions that go beyond b = 3 are ultimately not used for the main discussion sections, the existence of these values are interesting from a mathematical standpoint and highlight a major finding from the study that a and b are highly correlated. Further, provided a and b are properly correlated there is not anything necessarily unphysical about values of b $>$ 3 (a value of b $>$ 3 does not mean that the TWC is greater than that of a sphere over the size range of measured particles provided the a is appropriately chosena corollary of this would be a different way in which the density varies with the size of the particles). Therefore, we did not delete the text that the reviewer suggested we delete.

Major comment #7: Use PSD number uncertainty of 50% for larger particles and calculate associated TWC_{SD} uncertainty.

Response: Please see the response to Reviewer 2's major comment #5 as this point is addressed there.

Major comment #8: Likewise Z_{SD} uncertainty from Z equation that you have to present. See comment above.

Response: Please see the response to Reviewer 2's major comment #5 as this point is addressed there.

Major comment #9: How supercooled water has been quantified? Excluded from analysis? Be aware of the fact that Nevzorov will not correctly quantify LWC when IWC is more or less dominating TWC.

Response: We only use ice-phase measurements in our analysis and exclude all liquid-phase and mixed-phase periods from the work. We did this by removing all points from the analysis (rather than attempt to determine the IWC in a mixed-phase cloud) if the concentration from the CDP exceeded 10 cm^{-3} for any 1-s period during the 10 second interval. This is addressed in line 18 on page 4.

Text: To further constrain the study to periods when clouds were dominated by ice phase hydrometeors such that $TWC \approx IWC$ and to reduce the impact of liquid phase hydrometeors on the derived TWC and Z, observations were excluded from the analysis if the concentration from the cloud droplet probe exceeded 10 cm^{-3} at any point during the 10 s interval which usually corresponds to the presence of water (Heymsfield et al., 2011).

Major comment #10: Please document average number and mass PSD (additional figure!) for table 1 flight sequences.

Response: A figure has been added (Fig. 11 in the revised manuscript) that details the mean *N(D)* and the mean cumulative *M(D)* for each flight leg in this study, and is mentioned in line 11 on page 13 and referenced throughout Sect. 5.3.

Text: Figure 11 shows the mean *N(D)* and cumulative mass distribution function *M(D)* using the modified BF95 relationship for each flight leg analyzed in this study.

Major comment #11: Nevzorov *TWC* uncertainty: In literature several times has been documented that 2DC+2DP is matching the shallow Nevzorov *TWC*. Likewise for the deep cone in other publications. This illustrates that *a* and *b* coefficients can be adapted to match *TWC* from instruments, but it does not prove that shallow or deep cone Nevzorov collect ice at 100%. May be something between 50-100% for the deep cone. Check literature. Thus, the manuscript has to take into account possible systematic uncertainties of PSD number, Nevzorov TWC, and also measured *Z* impacting the tolerance of EPS and finally guiding recommendations of most likely *a* and *b* coefficients.

Response: Please see the response to Reviewer 2's major comment #5 as the Nevzorov *TWC* uncertainty is quantitatively addressed there. The issue of particle bounce out is also acknowledged there.

Major comment #12: Figure 9: if the underlying dataset would be statistically a little more representative (which is certainly not the case) wouldn't we expect more organized colours (contour plot gradient) perpendicular to the diagonal line of the grey matrix elements?

Response: The reviewer brings up a fair point. Trends in these values may be clearer if computation of the overlap region did not use a fine resolution of (a,b) values within the domain described in Sect. 3, or if there was a more statistically representative sample. Additionally, text has been added to lines 15–21 on page 12 to clarify instances where the percentage of overlap between two flight legs may not be the same.

Text: Thus, it is possible for the percentage of overlap between two flight legs to be greater when normalized by an equally plausible surface that is smaller in area, and a smaller degree of overlap when normalized by a larger equally plausible surface. It is worth noting that the percentage of overlap does not always follow an organized trend with respect to moving away from the gray diagonal line in the matrix as depicted in the top right corner of Fig. 9a. The lack of organized overlap values in some regions of the matrix could be influenced by the sensitivity in computing the overlap region over a fine resolution of (a,b) values within the domain described in Sec. 3, or perhaps could change in a more organized manner if there was a more statistically representative sample for these calculations to be made.

Major comment #13: 20 May flight: these are solely 'low altitude' data with T>-23, whereas for the other two flights used in this study, temperature T<-22. What is the argument to choose the 20 May flight since limited comparison with colder temperature data of two other flights?

Response: Inclusion of the 20 May event provided an additional environment for this study as airborne measurements were taken within the trailing stratiform region on this day. While the coldest temperature flight leg (an altitude of 7.9 km) is warmer than the coldest environment from the other two events (8.3–9.1 km in height), there remains a clear temperature dependence on the derived equally plausible surfaces. A brief rationale explaining why these particular events were chosen has been added to lines 21–22 on page 10.

Text: These particular events were chosen because of variations in how the complex of storms evolved and the location of in situ measurements relative to the convective system.

Minor comment #1: Pg 1, line 18: It does not make sense to establish m-D relation in mixed phase clouds. We know m-D for water droplets. You should exclude all mixed phase sequences from data!

Response: We agree with the reviewer and tried to better clarify what we did. Periods whereLWC was suspected to represent a notable component of the TWC were removed from the analysis, with stringent criteria developed to avoid notable contributions from supercooled water. Please see how this is detailed in the response to Reviewer 2's major comment #9. Further, explicit reference to mixed phase clouds has been removed from the last sentence in the abstract (line 18 on page 1) so that any confusion is avoided.

Text: These findings show the importance of representing the variability in a,b coefficients for numerical modeling and remote sensing studies rather than assuming fixed values, as well as the need to further explore how these surfaces depend on environmental conditions in clouds containing ice hydrometeors.

Minor comment #2: Figure 1 is not thoroughly documented with literature references and thus not reproducible.

Response: A supplemental table of these references (separate from the manuscript) has been added that includes the coefficients themselves, the environment and method in which they were derived, and pertinent notes. This table is mentioned in line 10 on page 2.

Minor comment #3: Pg 4, line 14: redo analysis with CDP droplet probe not exceeding 10 cm^{-3} on a 1 s basis may be a more suitable approach.

Response: The analysis has been redone using a threshold based on the 1 HZ CDP data, and is mentioned in line 21 on page 4 and also in the response to Reviewer 2's major comment #9.

Minor comment #4: Pg 4, line 18 ff: Assuming that S band radar reflectivity is not significant for sub-millimetric particles, what is the TWC percentile at 1mm of the cumulative mass PSD ? Please don't use B&F but for example Heymsfield 2010, etc.. retrieved for D_{max} definition.

Response: Figs. 11d-f in the revised manuscript provide the information necessary to determine estimates of the TWC percentile at 1 mm for each flight leg. As mentioned in response to the previous comments, clarifying that the BF95 coefficients were modified following Hogan et al. (2012) should address the reviewer's concern of an appropriate m-D relation for the derived cumulative *M(D)*.

Minor comment #5: Pg 8, line 14: 85 cm?

Response: The largest possible D that has particle masses (from the a and b at the 95th percentile in Fig. 4) less than those of spherical particles with a density of solid ice for the same D is computed by rearranging the equation $\rho_{ice} = (aD^b)/(\pi/6 \times D^3)$. This calculation is intended to merely reiterate the point in the previous sentence of the manuscript that "bulk variables such as Z derived using $b > 3$ are physically plausible only when the coefficients are applied over the range of particle sizes observed...". After addressing Reviewer 2's major comment #5, the a and b at the 95th percentile now permit a D as large as 3.83 cm.

Minor comment #6: Pg 9, line 26: Use m-D relation, for mass content estimation, other than BF95 for D_{max} size definition.

Response: Please see the response to Reviewer 2's major comment #3 as this point is fully addressed there.

Minor comment #7: Pg 11, line 5; Fig 11: Idem

Response: Please see the response to Reviewer 2's major comment #3 as this point is fully addressed there.

Minor comment #8: Pg 15, line 15 idem

Response: Please see the response to Reviewer 2's major comment #3 as this point is fully addressed there.

Minor comment #9: Pg 11, line 12; You mean just Fig 11 in this sentence?

Response: Figures 10–12 are all ordered the same as in Fig. 6, with "instances of multiple legs having the same average temperature shown in chronological order."

Minor comment #10: Pg 11, equation 6: How sphericity results deviate when comparing two instruments of different pixel resolution having sampled the same paricle? And how the averaging of sphericity has been performed over all crystals of a crystal population? For OAP 2D images the sphericity is size dependent, partly due to bias of 2D projections sorted into size classes, with larger particles having smaller 2D image sphericity than smaller particles.

Response: It is true that the probe resolution can cause differences in the computed sphericity, particularly at smaller particle sizes. However, the diode resolution is much less sensitive to sphericity as larger sizes are approached. Simple calculations of sphericity were conducted at 1.0 mm (the size at which the *N(D)* was found to agree within 5% between the 2D-C and HVPS during MC3E) that used a synthetically-generated spherical particle based on the probe resolution of the 2D-C and HVPS. At 1.0 mm, the percent difference in maximum sphericity between the HVPS and 2D-C is only 4.8%. The maximum sphericity for a circular particle was also computed using the HVPS resolution for larger sizes and found to vary by 6.8% between 1 mm and 10 mm. As such, the effect of diode resolution and particle size suggest that sphericity can be used as a quantitative comparison between flight legs for the points addressed in the manuscript.

Minor comment #11: Pg 12 line 16: Why applying factor 0.6 in reference volume for retrieving effective density, impacting TWC???

Response: Since most of the observed ice hydrometeors are non-spherical, the volume used in deriving effective density here applies the assumption that particles are enclosed by an oblate spheroid with a typical aspect ratio of 0.6 following observations from previous studies (e.g., Hogan et al., 2012). This point has been clarified in line 28 on page 14.

Text: The ρ_e, defined here as the ratio of TWC derived assuming the modified BF05 relationship to the integrated volume of particles enclosed by an oblate spheroid with an aspect ratio of 0.6 (e.g., Hogan et al., 2012), is estimated to evaluate its influence on TWC and Z.

A novel approach to characterize the variability in mass-Dimension relationships: results from MC3E

Joseph A. Finlon[1], Greg M. McFarquhar[2,3], Stephen W. Nesbitt[1], Robert M. Rauber[1], Hugh Morrison[4], Wei Wu[2], and Pengfei Zhang[2,5]

[1]Department of Atmospheric Sciences, University of Illinois at Urbana-Champaign, Urbana, IL 61801, United States
[2]Cooperative Institute for Mesoscale Meteorological Studies, University of Oklahoma, Norman, OK 73072, United States
[3]School of Meteorology, University of Oklahoma, Norman, OK 73072, United States
[4]National Center for Atmospheric Research, Boulder, CO 80301, United States
[5]NOAA/National Severe Storms Laboratory, Norman, OK 73072, United States

Correspondence: Greg M. McFarquhar (mcfarq@ou.edu)

Abstract. Mass-dimension (*m-D*) relationships determining bulk microphysical properties such as total water content (*TWC*) and radar reflectivity factor (*Z*) from particle size distributions are used in both numerical models and remote sensing retrievals. The *a* and *b* coefficients representing $m = aD^b$ relationships, however, can vary significantly depending on meteorological conditions, particle habits, definition of particle maximum dimension, the probes used to obtain the data, techniques used to process the cloud probe data, and other unknown reasons. Thus, considering a range of *a,b* coefficients may be more applicable for use in numerical models and remote sensing retrievals. Microphysical data collected by two-dimensional optical array probes (OAPs) installed on the University of North Dakota Citation aircraft during the Mid-latitude Continental Convective Clouds Experiment (MC3E) were used in conjunction with *TWC* data from a Nevzorov probe and ground-based S-band radar data to determine *a* and *b* using a technique that minimizes the chi-square difference between *TWC* and *Z* derived from the OAPs and that directly measured by a *TWC* probe and radar. All *a* and *b* within a specified tolerance were regarded as equally plausible solutions. Of the 16 near-constant temperature flight legs analyzed during the 25 April, 20 May, and 23 May 2011 events, the derived surfaces of solutions on the first two days where the aircraft sampled stratiform cloud had a larger range in *a* and *b* for lower temperature environments that ~~corresponded~~ correspond to less variability in *N(D)*, *TWC*, and *Z* for a flight leg. Because different regions of the storm were sampled on 23 May, differences in the variability of *N(D)*, *TWC*, and *Z* influenced the distribution of chi-square values in (*a,b*) phase space and the specified tolerance in a way that yielded ~~6.7~~ 2.8 times fewer plausible solutions compared to the flight legs on the other dates. These findings show the importance of representing the variability in *a,b* coefficients for numerical modeling and remote sensing studies rather than assuming fixed values, as well as the need to further explore how these surfaces depend on environmental conditions in ~~ice and mixed phase clouds~~ clouds containing ice hydrometeors.

1 Introduction

Mass-dimension (*m-D*) relations are required to link bulk microphysical properties, such as total water content (*TWC*) and forward model radar reflectivity factor (*Z*), to ice crystal particle size distributions (PSDs). These relations are extensively assumed in both numerical models and remote sensing retrievals and relate a particle's mass (*m*) to its size, typically defined by its maximum dimension projected onto a 2-D plane (*D*), by means of a power law in the form $m = aD^b$. Past studies have suggested the exponent *b* is related to the exponent in surface area-dimension relationships (Fontaine et al., 2014) or to a particle's fractal dimension (Schmitt and Heymsfield, 2010). The prefactor *a* has some dependence on *b* and on the particle density.

Prior *m-D* relationships have been determined using cloud probe data obtained in a variety of environmental conditions. Figure 1a shows how *m-D* coefficients derived from previous studies vary depending on the types of clouds sampled. A full list of these *m-D* coefficients and their corresponding references is available as a supplement. Coefficients derived using data over mountainous terrain (e.g., Nakaya and Terada, 1935; Locatelli and Hobbs, 1974), cirrus clouds (e.g., Heymsfield, 1972; Hogan et al., 2000), convective clouds (e.g., Liu and Curry, 2000; Cazenave et al., 2016; Leroy et al., 2016), regions of large scale ascent (e.g., Szyrmer and Zawadzki, 2010), and computer-generated shapes (e.g., Matrosov, 2007; Olson et al., 2016) are shown. A total of 119 relations are shown in Fig. 1. The range of *a* in Fig. 1a spans five orders of magnitude, with variations in *a* spanning 3 orders of magnitude or more even for measurements obtained in the same cloud type. The exponent *b* ranges between one and three within the same environments. The relations in Fig. 1 were derived using data collected by different types and versions of cloud probes, using different algorithms to process the data. McFarquhar et al. (2017) have shown that it can be difficult to disentangle the dependence of derived microphysical parameters on environmental conditions from the dependence on the probes used to collect and the methods to process the data.

Figure 1b shows that *m-D* coefficients also vary depending on the technique used to derive the *m-D* relations. In some studies the maximum dimension of frozen hydrometeors was recorded before the crystal was melted and the single particle mass subsequently measured (Magono and Nakamura, 1965; Zikmunda and Vali, 1972; Mitchell et al., 1990), whereas other studies used measurements of either bulk mass measured by an evaporation probe (Heymsfield et al., 2002; Cotton et al., 2013; Xu and Mace, 2017) or bulk Z observed by a collocated radar measurement ~~(McFarquhar et al., 2007b; Maahn et al., 2015)~~ (McFarquhar et al., 2007a; Maahn et al., 2015) in combination with in situ measured PSDs. Further, Wu and McFarquhar (2016) showed inconsistencies in how *D* is defined (Mitchell and Arnott, 1994; Brown and Francis, 1995; McFarquhar and Heymsfield, 1996; Heymsfield et al., 2013; Lawson et al., 2015; Korolev and Field, 2015) can also impact *m-D* relations. For example, they noted ice water content (*IWC*) values derived using various definitions of *D* ranged between 60 and 160% of the *IWC* derived using a smallest enclosing circle to define *D*.

Remote sensing retrieval schemes and model microphysical parameterization schemes are sensitive to the choice of *m-D* relationship. For example, Delanoë and Hogan (2010) showed that differences in the mean extinction, *IWC*, and effective radius retrieved from spaceborne remote sensors were 28, 9, and 30%, respectively, depending on whether *m-D* relations of spherical aggregates (Brown and Francis, 1995, hereafter BF95) or bullet rosettes (Mitchell, 1996) were used. McCumber et al. (1991) showed time series of modeled precipitation rate with differences of 20 to 50% depending on assumptions about particle density, which are affected by the *m-D* relation. Later studies (e.g., Mitchell, 1996; Erfani and Mitchell, 2016) attributed differences in model output to the influence of particle mass on terminal fall velocities.

Although many studies have established *m-D* relations for specific cases, a universal *m-D* relationship has not been found nor can a single relation be expected to represent the wide range of crystal habits and sizes within clouds occurring at different temperatures, locations, or formed by different mechanisms. Moreover, a single relationship cannot account for the natural variability of cloud properties such as particle size, shape, and density that occurs even in similar environmental conditions. Thus, some alternate approach is more appropriate for modeling and remote sensing studies that considers multiple *m-D* relations over many retrievals or model simulations to evaluate the variability in the ensemble results.

While previous studies (e.g., McFarquhar et al., 2007b; Heymsfield et al., 2010; Mascio et al., 2017) have considered how *m-D* relations vary with environmental conditions, such as temperature, the derived relations were fixed regardless of potential fluctuations for that environment. Further uncertainties were associated with measurement errors induced by shattering of large ice crystals on probe tips and subsequent detection within the probe's sample volume (Field et al., 2003), the processing techniques used (McFarquhar et al., 2017), and from the statistical counting of particles (e.g., Hallett, 2003; McFarquhar et al., 2007a). The approach by Fontaine et al. (2014) evaluated the variability in the prefactor *a* for an assumed exponent *b* for two field projects, but ultimately still derived a single *m-D* relationship for each dataset based on the mean conditions.

Extending the approach of McFarquhar et al. (2015), which derived a volume of equally realizable solutions within the phase space of the three gamma fit parameters (concentration N_0, shape μ, and slope λ) characterizing PSDs, a novel approach is used here to determine equally valid *m-D* relations for a given environment. Data from a variety of environments sampled during the Mid-latitude Continental Convective Clouds Experiment (MC3E) are used to establish a surface of equally plausible *a* and *b* coefficients in (*a,b*) phase space using a technique that minimizes the chi-square difference between the *TWC* and *Z* derived from the PSDs measured by optical array probes (OAPs) and that directly measured by a *TWC* probe and radar.

The remainder of this paper is organized as follows. Section 2 outlines the datasets used and the methodology to process the radar and microphysics data, while Sect. 3 describes the technique employed to determine the surfaces of *m-D* coefficients. A brief description of the MC3E cases used in this study is provided in Sect. 4, and the surfaces of coefficients are derived and discussed in Sect. 5. A summary of the technique and its implications for numerical modeling and remote sensing retrieval schemes are given in Sect. 6.

2 Data and methodology

The data in this study were collected within mesoscale convective systems (MCSs) during the 2011 Mid-latitude Continental Convective Clouds Experiment (MC3E; Jensen et al., 2016). The study presented here uses data from cloud microphysical instruments aboard the University of North Dakota (UND) Cessna Citation II aircraft and from the Vance Air Force Base, OK (KVNX) Weather Surveillance Radar-1988 Doppler (WSR-88D) radar.

2.1 Identification of coincident aircraft/radar data

The use of airborne microphysical measurements and radar data collected from the ground allowed sampling of the same region of the cloud from microphysical and remote sensing perspectives. Use of the Airborne Weather Observation Toolkit (https://github.com/swnesbitt/AWOT) radar matching algorithm and the Python ARM Radar Toolkit (Py-ART; Helmus and Collis, 2016) permitted calculation of radar *Z* in the vicinity of the aircraft for each second of in situ cloud distributions measured during flight. The algorithm organizes all radar gates in a 3-Dimensional space (Maneewongvatana and Mount, 1999) for efficient acquisition of radar parameters at nearby radar range gates. The Barnes (1964) interpolation technique is then applied to data at the eight nearest gates within 500 m of the aircraft's location, ignoring vertically adjacent gates beyond a range of 65 km as the beamwidth exceeds the 500 m threshold, to obtain an averaged *Z* at the aircraft location.

To compare microphysical properties with radar-measured Z for constant altitude flight legs at similar environmental temperature, only those times when the radar and microphysical datasets are coincident and the temperature varies by less than 1 °C were considered. To reduce uncertainty due to counting statistics in the measured PSDs, microphysical data were averaged over a 10 s period. Each 10 s period determined required radar echo and microphysical data for all 1 s samples to ensure that the aircraft and matched radar Z were completely in cloud during the 10 s period. The *TWC* measurements and matched radar *Z* were then averaged over the same 10 s period, with each 10 s interval assigned as a coincident point. Table 1 lists the start and end times, mean altitude, and temperature for each of the 16 constant-temperature flight legs flown when the UND Citation was in cloud. Observations where the mean *TWC* for ~~each~~ a 10 s interval < 0.05 g m^{-3} were ignored as the values were considered either below the noise threshold of the Nevzorov probe or optically thin cloud. To further constrain the study to periods when clouds were dominated by ice phase hydrometeors such that *TWC* ≈ *IWC* and to reduce the impact of liquid phase hydrometeors on the derived *TWC* and *Z*, observations were excluded from the analysis if the ~~10 mean~~ concentration from the cloud droplet probe exceeded 10 cm^{-3} at any point during the 10 s interval which usually corresponds to the presence of water (Heymsfield et al., 2011). Of the coincident observations considered, ~~12.3~~13% were excluded from the analysis based on these criteria. A total of ~~493~~ 489 coincident observations were retained for this analysis.

2.2 Radar measurements

Data from the KVNX S-band (10 cm wavelength) radar were used in this study. Although the NASA dual-polarization (N-Pol) S-band Doppler radar was deployed during MC3E, mechanical issues prevented reliable collection of data for two of the three events examined here. Radars at other wavelengths collected data during MC3E. However, attenuation through liquid portions of the cloud (e.g., Bringi et al., 1990; Park et al., 2005; Matrosov, 2008) and non-Rayleigh scattering by larger particles (e.g., Lemke and Quante, 1999; Matrosov, 2007) could not be accounted for, and prompted exclusive use of the S-band radar.

Radar reflectivity factor values for gates near the UND Citation (Sect. 2.1) were used to obtain the average value of *Z* using the radar matching algorithm only if the following criteria were met: correlation coefficient $\rho_{HV} \geq 0.75$, sigma differential phase *SDP* $\leq$ 12 deg^2 km^{-2}, differential reflectivity -2 $\leq Z_{DR} \leq$ 3 dB, and reflectivity texture (defined as the standard deviation in *Z* of the nearest 5 gates) $<$ 7 dBZ. These ranges represent acceptable values for echoes based on previous studies

(Bringi and Chandrasekar, 2001). Radar gates not meeting these criteria were masked, reducing the likelihood of including gates with excessive signal noise due to clutter or weak signal, contamination by the aircraft, or other factors. For instances where the matched Z changed by more than 2 dBZ for subsequent 1 s points (fewer than one percent of the observations), all radar gates factored into the radar matching algorithm were inspected by eye to ensure that no outlier values were responsible for the jump in the matched Z. Of the observations that were manually inspected, all appeared spatially consistent with no outliers present, and as such remained in the averaging routine of the matching algorithm discussed in Sect. 2.1.

2.3 Microphysical measurements

During MC3E the Citation aircraft sampled clouds in situ, with most data collected in ice phase clouds between the melting layer and cloud top (Jensen et al., 2016). A suite of microphysical instruments was installed on the aircraft, including OAPs, which were used to image particles and derive PSDs, and a TWC probe. Specifics on the instrumentation and steps used to process the data are described below.

2.3.1 OAP data

A cloud imaging probe (CIP), a 2D cloud (2D-C) probe, and a High Volume Precipitation Spectrometer Version 3 (HVPS-3) sized particles by shadowing photodiode arrays attached to fast response electronics. Data from the 2D-C and HVPS-3 were combined to create a composite PSD, permitting particles between 150 µm and 19.2 mm to be considered in the analysis. The 2D-C was used instead of the CIP in the analysis even though the CIP has a larger sample volume because the inclusion of anti-shattering tips on the 2D-C reduced the impact of shattered artifacts (e.g., Korolev et al., 2011). Previous studies (Korolev et al., 2011, 2013a; Jackson et al., 2014) have shown that use of algorithms to identify shattered artifacts are sometimes needed even when the OAP is equipped with anti-shattering tips. Artifacts are identified by examining the frequency distribution of the times between which particles enter the sample volume (inter-arrival time; Field et al., 2006). When artifacts are present, this distribution follows a bimodal distribution with naturally-occurring particles having a mode with longer inter-arrival times and shattered artifacts having a mode with shorter inter-arrival times (e.g., Field et al., 2003). During MC3E there was only one mode in the inter-arrival time distribution corresponding to the naturally-occurring particles (Wu and McFarquhar, 2016) at all times, suggesting there were few shattered artifacts. Therefore, no shattering removal algorithm was used for the 2D-C and HVPS. Following Wu and McFarquhar (2016), the number distribution function *N(D)* was ~~obtained~~ determined using the 2D-C for particles with $D < 1$ mm and the HVPS-3 for $D > 1$ mm. The 1 mm cutoff was chosen since *N(D)* ~~between~~ for the two OAPs agreed on average within 5 percent for $0.8 \leq D \leq 1.2$ mm, and was used for all PSDs irrespective of periods when the difference between *N(D)* for the OAPs exceeded 5% in the overlap region. Given uncertainties in the probe's sample area and limitations of its depth of field for smaller particle sizes (Baumgardner and Korolev, 1997), particles with $D < 150$ µm were not included in the analysis.

The OAP data were processed using the University of Illinois/Oklahoma OAP Processing Software (UIOOPS; McFarquhar et al., 2018). Numerous morphological properties were calculated (e.g., particle maximum dimension, projected area, perimeter, area ratio, and habit) for individual particles, and PSDs were determined for each second of flight. Following Heymsfield and Baumgardner (1985) and Field (1999), only particles ~~with a center of mass~~ imaged with their center within the OAP's field of view were considered as otherwise there is too much uncertainty in particle ~~shape. Shattered artifacts were removed using a threshold for the required time between particles entering the sample volume (inter-arrival time; Field et al., 2006). The inter-arrival times typically follow a bimodal distribution, with naturally-occurring particles having a mode with longer inter-arrival times and shattered artifacts having shorter inter-arrival times (e.g., Field et al., 2003). A constant inter-arrival time threshold of 10^{-5} was applied to the 2D-C data, with particles below this threshold identified as artifacts~~size. Particles were identified as having their center within the field of view if their maximum dimension along the time direction exceeded the largest length where the particle potentially touched the edge of the photodiode array.

2.3.2 TWC data

The *TWC* was determined from the Nevzorov probe using the power required to melt or evaporate ice particles impinging on the inside of a cone (e.g., Nevzorov, 1980; Korolev et al., 1998). The probe used had a deeper cone than previous designs with a 60° vertex angle (as opposed to a 120° angle) that prevented many particles from bouncing out of the cone. Because previous studies suggested that particles with $D > 4$ mm can bounce out of even the deeper cone (Wang et al., 2015), *TWC* may be underestimated when such particles are present. However, Korolev et al. (2013b) showed that the ratio of the Nevzorov *IWC* to that derived from the measured PSDs using the BF95 relation did not significantly vary with particle maximum dimension. Of the coincident points belonging to constant altitude flight legs in this study, 79.2% of the observations had cumulative mass estimates using the BF95 relation from particles with $D \leq 4$ mm contributing at least 80% to the total mass. Therefore, measurements of *TWC* were included irrespective of whether $D_{\text{max}} > 4$ mm.

3 Development of equally plausible (*a,b*) surfaces

In this section, a method for determining a surface of equally realizable solutions for *m-D* coefficients in the phase space of (*a,b*) coefficients is described. The surface of these coefficients is determined through a procedure that minimizes the χ^2 differences between the *TWC* and *Z* derived from *N(D)* and that directly measured by the Nevzorov and ground-based radar, respectively. The minimization procedure is carried out for each constant-temperature flight leg (defined by temperature varying by less than 1 °C) for the MC3E cases studied. This approach follows that of McFarquhar et al. (2015) who developed volumes of equally realizable N_0, μ, and λ characterizing observed *N(D)* as gamma distributions for observations obtained during the Indirect and Semi-Direct Aerosol Campaign (ISDAC) and the NASA African Monsoon Multidisciplinary Analyses project (NAMMA).

For an individual 10 s sample, the *TWC* and *Z* derived from the PSD for a specific *a* and *b* is given by TWC_{SD} and Z_{SD}, respectively, as

$$TWC_{\text{SD}} = \sum_{j=1}^{N} (aD^b) N(D_j) dD_j \text{ and} \tag{1}$$

$$Z_{\mathrm{SD}} = \left(\frac{6}{\pi \rho_{ice}}\right) \frac{|K_{ice}|^2}{|K_w|^2} \sum_{j=1}^{N} (aD^b)^2 N(D_j) dD_j \tag{2}$$

following the method of Hogan et al. (2006) and accounting for the different dielectric constants for water ($|K_w|^2 = 0.93$) and ice ($|K_{ice}|^2 = 0.17$). Uncertainties in TWC_{SD} and Z_{SD} are discussed later in this section. The metric defining the difference between the *TWC* and *Z* derived from *N(D)* for a specific *a* and *b* and that directly measured by the Nevzorov and ground-based radar, respectively, is given by TWC_{diff} and Z_{diff} as follows:

$$TWC_{\mathrm{diff}} = \left[\frac{TWC - TWC_{\mathrm{SD}}(a,b)}{\sqrt{TWC \times TWC_{\mathrm{SD}}(a,b)}}\right]^2 \text{ and} \tag{3}$$

$$Z_{\mathrm{diff}} = \left[\frac{\sqrt{Z} - \sqrt{Z_{\mathrm{SD}}(a,b)}}{\sqrt{\sqrt{Z} \times \sqrt{Z_{\mathrm{SD}}(a,b)}}}\right]^2 . \tag{4}$$

In this study, TWC_{diff} and Z_{diff} are computed for all points in the domain of values encompassing $5 \times 10^{-4} < a < 0.35$ g cm$^{-\mathrm{b}}$ and $0.20 < b < 5.00$ at increments of 5×10^{-4} g cm$^{-\mathrm{b}}$ and 0.01, respectively. The

Given a priori assumptions of *Z* being proportional to the square of a particle's mass, the square root of reflectivity was used in Eq. (4) so that TWC_{diff} would be similar to Z_{diff} on average and each would have approximately equal weight in determining *a* and *b*. Although radar *Z* measurements involve a significantly greater sample volume than that of OAPs and a bulk content probe, TWC_{diff} and Z_{diff} were not weighted proportionally to the sample volume in order to ensure that both bulk moments had some impact on the derived *a* and *b*. Given that larger ice crystals are fractionally more important than small crystals in determining Z_{SD} than TWC_{SD} and given varying contributions of larger crystals to Z_{SD} and TWC_{SD}, TWC_{diff} has a greater impact on the χ^2 minimization procedure some of the time while Z_{diff} does at other times. The ratios between Z_{diff} and TWC_{diff} for each flight leg are given in Table 2, and range between 0.32 and 8.58 with a mean of 2.62 for the 16 flight legs. No attempt is made to force equal weight for Z_{diff} and TWC_{diff} for each coincident point because there are periods when cloud properties influence *TWC* differently than *Z*.

At first, the sum of $TWC_{\mathrm{diff}} + Z_{\mathrm{diff}}$ is used to identify ($K_{ice}|^2 = 0.17$) *a,b*) values that characterize an individual 10 s data point. An example of TWC_{diff} and + Z_{diff} values computed in (*a,b*) phase space for a 10 s averaged PSD measured beginning at 13:56:45 UTC on 20 May 2011 is shown in Fig. 2a. The color representing $TWC_{\mathrm{diff}} + Z_{\mathrm{diff}}$ is shaded on a logarithmic scale to more easily show the range of values. The smallest swath of values, arbitrarily chosen as being $TWC_{\mathrm{diff}} + Z_{\mathrm{diff}} \leq 1$ within the region outlined black, spans *b* values of 1.13 to 4.72. The curvature in the outlined region highlights the correlation of *a* and *b* so showing that similar *m* can be obtained from using very different *b* by adjusting *a* accordingly. Considering both TWC_{diff} and Z_{diff} allows the shape and placement of the smallest swath of values to adjust according to two different moments of the PSD since conditions impact *TWC* differently than *Z*. Using two constraints on the χ^2 minimization technique therefore provides additional insight into the microphysical properties as discussed in Sect. 5.

The chi-square statistic for a flight leg, defined as

$$\chi^2(a,b) = \frac{1}{N}\sum_{i=1}^{N}\left[TWC_{\text{diff}}(i) + Z_{\text{diff}}(i)\right], \tag{5}$$

involves a summation over all N 10 s coincident observations represented by the index i and normalized by N. When χ^2 is computed by summing over all N points in the flight leg, the region with the smallest χ^2 ($\chi^2 \leq 1$; outlined region in Fig. 2b) is smaller than the region in Fig. 2a which shows χ^2 for a single point, because different (a,b) minimize χ^2 for each of the individual PSDs in the 5 minute period depicted. Therefore, overall the χ^2 values are higher than the $TWC_{\text{diff}} + Z_{\text{diff}}$ computed for each (a,b). The point in Fig. 2b shows corresponds to the a and b point that minimizes χ^2, hereafter represented as χ^2_{min}, which represents the most likely a and b valuesvalue.

To represent the uncertainty in the derived coefficients for each flight leg, all a and b fulfilling $\chi^2 \leq \chi^2_{\text{min}} + \Delta\chi^2$ are assumed to be equally plausible solutions. McFarquhar et al. (2015) defined Analagous to McFarquhar et al. (2015), the confidence region is defined as $\Delta\chi^2 = \max($$\chi^2_{\text{min}}$, $\Delta\chi^2_1$, χ^2_{min}), where $\Delta\chi^2_2$). The χ^2_{min} characterizes the robustness of the minimization procedure affected by the natural parameter variability over a flight leg, $\Delta\chi^2_1$ represented represents uncertainties in the PSD due to statistical sampling uncertaintiesand χ^2_{min} characterized the robustness of the minimization procedure, and $\Delta\chi^2_2$ represents measurement uncertainties. Similar to their study, $\Delta\chi^2_1$ is determined here as

$$\Delta\chi^2_1 = \frac{1}{N}\sum_{i=1}^{N} \begin{array}{l} \frac{1}{2}\left\{\left[\frac{TWC_{\text{SD,min}}(i) - TWC_{\text{SD}}(i)}{\sqrt{TWC_{\text{SD,min}}(i)\times TWC_{\text{SD}}(i)}}\right]^2 + \left[\frac{\sqrt{Z_{\text{SD,min}}(i)} - \sqrt{Z_{\text{SD}}(i)}}{\sqrt{\sqrt{Z_{\text{SD,min}}(i)}\times\sqrt{Z_{\text{SD}}(i)}}}\right]^2\right\} + \\ \frac{1}{2}\left\{\left[\frac{TWC_{\text{SD,max}}(i) - TWC_{\text{SD}}(i)}{\sqrt{TWC_{\text{SD,max}}(i)\times TWC_{\text{SD}}(i)}}\right]^2 + \left[\frac{\sqrt{Z_{\text{SD,max}}(i)} - \sqrt{Z_{\text{SD}}(i)}}{\sqrt{\sqrt{Z_{\text{SD,max}}(i)}\times\sqrt{Z_{\text{SD}}(i)}}}\right]^2\right\}. \end{array} \tag{6}$$

The different terms in Eq. (6) represent the difference in the minimum and maximum TWC or Z derived from the minimum and maximum *N(D)* using the most likely (a,b) minimizing χ^2 ($TWC_{\text{SD,min}}$ and $TWC_{\text{SD,max}}$ or $Z_{\text{SD,min}}$ and $Z_{\text{SD,max}}$) and that derived from the most likely measured *N(D)* (TWC_{SD} or Z_{SD}). Following McFarquhar et al. (2015), the minimum and maximum *N(D)* are determined by subtracting or adding the square root of the number of particles counted in each size bin to the number of particles counted in the bin when computing *N(D)*. This technique represents uncertainty in the actual particle counts for each size bin as given by Poisson statistics (Hallett, 2003; McFarquhar et al., 2007a).

Estimates of the measurement uncertainty from the OAPs, Nevzorov probe, and ground-based radar also influence the uncertainty in the derived coefficients. The uncertainty due to measurement error $\Delta\chi^2_2$ is defined as

$$\Delta\chi^2_2 = \frac{1}{N}\sum_{i=1}^{N} \begin{array}{l} \frac{1}{2}\left\{\left[\frac{TWC_{\text{SD,meas\_min}}(i) - TWC_{\text{SD}}(i)}{\sqrt{TWC_{\text{SD,meas\_min}}(i)\times TWC_{\text{SD}}(i)}}\right]^2 + \left[\frac{\sqrt{Z_{\text{SD,meas\_min}}(i)} - \sqrt{Z_{\text{SD}}(i)}}{\sqrt{\sqrt{Z_{\text{SD,meas\_min}}(i)}\times\sqrt{Z_{\text{SD}}(i)}}}\right]^2 + \left[\frac{TWC_{\text{meas\_min}}(i) - TWC(i)}{\sqrt{TWC_{\text{meas\_min}}(i)\times TWC(i)}}\right]^2 + \right. \\ \left. \left[\frac{\sqrt{Z_{\text{meas\_min}}(i)} - \sqrt{Z(i)}}{\sqrt{\sqrt{Z_{\text{meas\_min}}(i)}\times\sqrt{Z(i)}}}\right]^2\right\} + \frac{1}{2}\left\{\left[\frac{TWC_{\text{SD,meas\_max}}(i) - TWC_{\text{SD}}(i)}{\sqrt{TWC_{\text{SD,meas\_max}}(i)\times TWC_{\text{SD}}(i)}}\right]^2 + \left[\frac{\sqrt{Z_{\text{SD,meas\_max}}(i)} - \sqrt{Z_{\text{SD}}(i)}}{\sqrt{\sqrt{Z_{\text{SD,meas\_max}}(i)}\times\sqrt{Z_{\text{SD}}(i)}}}\right]^2 + \right. \\ \left. \left[\frac{TWC_{\text{meas\_max}}(i) - TWC(i)}{\sqrt{TWC_{\text{meas\_max}}(i)\times TWC(i)}}\right]^2 + \left[\frac{\sqrt{Z_{\text{meas\_max}}(i)} - \sqrt{Z(i)}}{\sqrt{\sqrt{Z_{\text{meas\_max}}(i)}\times\sqrt{Z(i)}}}\right]^2\right\}. \end{array} \tag{7}$$

The terms $TWC_{\mathrm{SD,meas\_min}}$, $TWC_{\mathrm{SD,meas\_max}}$, $Z_{\mathrm{SD,meas\_min}}$, and $Z_{\mathrm{SD,meas\_max}}$ represent the minimum and maximum *TWC* or *Z* derived using a 50% uncertainty in the measured *N(D)*. This uncertainty follows Heymsfield et al. (2013) where up to a 50% difference in the number concentration for particles with $D > 0.1$ mm was determined. Uncertainties in the bulk measurements of *TWC* and *Z* must also be considered in the generation of the uncertainty surfaces with the minimum and maximum possible bulk values represented as $TWC_{\mathrm{meas\_min}}$, $TWC_{\mathrm{meas\_max}}$, $Z_{\mathrm{meas\_min}}$, and $Z_{\mathrm{meas\_max}}$. Following Korolev et al. (2013b), it was assumed that there was a 2% uncertainty when $D_{\max} \leq 4$ mm and a 8% uncertainty for other periods to address the possibility of particles bouncing out of the cone of the Nevzorov probe. A radar reflectivity uncertainty of 1 dB (Krajewski and Ciach, 2003) is subtracted from or added to the measured *Z* to determine $Z_{\mathrm{meas\_min}}$ and $Z_{\mathrm{meas\_max}}$.

Figure 3 illustrates the frequency distribution of the ratio between $\chi^2_{\min}$ and $\Delta\chi^2_1$ (blue shading) and between $\chi^2_{\min}$ and $\Delta\chi^2_2$ (red shading) for all 16 flight legs. Of all 16 legs considered, 15 have a ratio between $\chi^2_{\min}$ and $\Delta\chi^2_1$ greater than 1, meaning $\chi^2_{\min} > \Delta\chi^2_1$~~and $\Delta\chi^2 = \chi^2_{\min}$~~, and 50% of the observations have ratios greater than 10. ~~This indicates~~ For 5 of the 16 legs, the ratio between $\chi^2_{\min}$ and $\Delta\chi^2_2$ is greater than 1 indicating that the χ^2 obtained from the (*a*,*b*) minimization procedure is greater than the difference between moments derived from the minimum and maximum *N(D)* ~~for nearly all~~ and from the minimum and maximum *TWC* and *Z* due to measurement errors for nearly a third of the periods in this study. This means that the natural parameter variability over a flight leg is ~~typically~~ sometimes more important for the derived uncertainty of *m-D* coefficients~~than is the uncertainty due to statistical counting~~, whereas at other times measurement errors are more important. This is further discussed in Sect. 5.

At first, the *b* coefficients greater than 3 shown in Fig. 2 may seem counter intuitive as the mass of a particle cannot be greater than that of an ice sphere. Further, a particle's density would increase with increasing *D* for $b > 3$. But, due to the covariability of *a* and *b*, $b > 3$ does not necessarily imply the particle has a mass greater than a sphere. Nevertheless, equally plausible *b* values greater than 3 were closely inspected as past studies (e.g., Fontaine et al., 2014) have disregarded $b > 3$ as a possible exponent in an *m-D* relation. To investigate the impact of $b > 3$, a linear sequence of *b* values in the plausible surface was generated for each flight leg and the 5$^{\text{th}}$, 25$^{\text{th}}$, 50$^{\text{th}}$, 75$^{\text{th}}$, and 95$^{\text{th}}$ percentiles of *b* were determined. The corresponding *a* from each of these *b* was identified, and the cumulative reflectivity distribution functions, defined as

$$Z_c(D) = \left(\frac{6}{\pi \times \rho_{\mathrm{ice}}}\right)^2 \frac{|K_{\mathrm{ice}}|^2}{|K_w|^2} \int_0^D (aD'^b)^2\, N(D')\, dD', \tag{8}$$

were computed using the mean *N(D)* for the period and the particle mass derived with these *a* and *b*. Figure 4 shows an example of the $Z_c(D)$ over the range of particle sizes observed from the -23 °C flight leg on 20 May 2011 using these *a* and *b* coefficients. ~~Although the~~ The $Z_c(D)$ derived using ~~the~~ BF95 coefficients, with the prefactor *a* ($= 0.002$ g cm$^{-1.9}$) modified following the correction factor of Hogan et al. (2012) applicable for the definition of *D* used here, is also shown for reference~~, it~~. It is worth noting that the modified BF95 coefficients may reasonably resolve the particle mass for *some* particle sizes for the PSD depicted in Fig. 4. While the lower values of *a* and *b* yield larger $Z_c(D)$ for smaller *D* than do the larger values of *a* and *b*, the derived total reflectivity $Z_t = \int_{D_{min}}^{D_{max}} Z(D)\, dD$ for the 5$^{\text{th}}$ and 95$^{\text{th}}$ percentiles of *b* are within ~~9.18~~ 11.38 mm^6 m^{-3} of the mean matched radar *Z* of 18.36 mm^6 m^{-3} (12.64 dBZ), a difference of ~~50~~ 62 percent of the mean. In contrast, the difference of the mean from the Z_t computed with modified BF95 coefficients is much higher, 88.6%, suggesting values of $b > 3$ are indeed giving plausible results for the range of particle sizes observed.

When the ~~six~~ seven flight legs that have some values of $b > 3$ in the surface of equally plausible solutions are considered, Z values for the 5$^{\text{th}}$ and 95$^{\text{th}}$ percentiles of b are within 82.4% of the mean matched radar Z. While this value is greater than the 50.5% difference for the other flight legs and for the period illustrated in Fig. 4, Z values for the 5$^{\text{th}}$ and 95$^{\text{th}}$ percentiles are more consistent with the mean matched radar Z compared to that computed with the modified BF95 relationship.

Thus, the bulk variables such as Z derived using $b > 3$ are physically plausible for the distributions examined here given the covariability of a and b. However, this conclusion may only apply when the coefficients are applied over the range of particle sizes observed during MC3E and assuming PSDs with similar shapes. For example, for the 95$^{\text{th}}$ percentile of b ($b =$ ~~3.32~~3.61) and the corresponding value of a used to construct Fig. 4, ice particles with $D <$ ~~85~~ 3.83 cm have particle masses less than those of spherical particles with a density of solid ice for the same maximum dimension. On the other hand, if the covariability of a and b was not taken into account when choosing the corresponding a value, then a particle could have a mass greater than that of a spherical particle for much smaller D. While the technique highlights the possibility of a wide range of m-D coefficients for a given environment, equally plausible solutions containing $b > 3$ are still not considered in the remainder of this study to remain consistent with previous studies and to avoid any chance of unphysical behavior should the equally plausible coefficients be ~~applied~~ extrapolated to PSDs from remote sensing retrievals or microphysics parameterization schemes that extend to particle sizes larger than in the original dataset.

4 Events overview

The Citation aircraft sampled different ice phase environments during the 25 April, 20 May, and 23 May 2011 flights. Jensen et al. (2016) provide an overview of all MC3E cases, while Jensen et al. (2014) give a synoptic scale overview of the MCSs examined in this study. These particular events were chosen because of variations in how the complex of storms evolved and the location of in situ measurements relative to the convective system. Figure 5 shows a 0.5° plan-position indicator (PPI) scan of corrected radar reflectivity from the KVNX radar for each event. The PPI was obtained during the middle of the UND Citation flight leg depicted by the black line in Fig. 5.

The first event involved an upper-level trough that produced ascent aloft and generated thunderstorms across northern Oklahoma around 06 UTC on 25 April 2011. As these storms traversed northward along an elevated frontal boundary overnight, their bases decoupled from the boundary layer as daytime solar radiation ceased. The discrete cells evolved into an MCS and moved into southern Kansas by 11 UTC (Fig. 5a) when the Citation sampled weaker embedded convection and broader stratiform precipitation. The second MCS, with a north-to-south oriented squall line which was part of a larger system, developed from a line of convective cells originating in west Texas along a dry line around 10 UTC on 20 May 2011 and propagated into the deployment region in north central Oklahoma. The Citation aircraft primarily flew within the trailing stratiform region of the MCS (Fig. 5b). The third MCS originated as a series of discrete supercell thunderstorms along a surface dry line in western

Oklahoma and moved eastward into the MC3E domain by 21 UTC on 23 May 2011 before transitioning to a more linear MCS feature. Microphysical measurements were made in the anvil region of these strong thunderstorms (Fig. 5c).

To provide context of the bulk characteristics sampled during each event, boxplots of Z matched at the aircraft's location and TWC from the Nevzorov probe for each constant-temperature flight leg are given in Fig. 6. The whiskers represent the 5^{th} and 95^{th} percentiles from coincident observations, the box edges denote the 25^{th} and 75^{th} percentiles, and the red line in the middle is the median. Distributions are listed in order of decreasing temperature, with instances of multiple legs having the same average temperature shown in chronological order. While the bulk TWC and Z may differ for flight legs of similar average temperature on a given day, as in the -26.5 and -35 $^{\circ}$C environments on 25 April (Figs. 6a-b), greater or smaller TWC correlates with greater or smaller Z for most cases. The variability in the TWC and Z as it relates to the construction of surfaces of equally plausible *m-D* coefficients is discussed in the next section.

5 Results

This section discusses how the *(a,b)* surfaces vary between different cases, as a function of temperature, depending on the determination of radar reflectivity, and depending on whether PSDs had large mass contributions from particles with $D > 4$ mm.

5.1 Radar absolute *Z* calibration

While S-band radars within the NEXRAD WSR-88D network are calibrated individually and among one another upon initial installation, biases in Z can develop over time (Ice et al., 2017). Zhang et al. (2013) described a technique that uses self-similarity in the Z, Z_{DR}, and specific differential phase (K_{DP}) fields to estimate the absolute Z bias for events in rain. This method was employed for the cases in this study and biases in Z of -1.08 (25 April), -0.65 (20 May), and 1.43 dBZ (23 May 2011) were found. These corrections were applied to the value of Z calculated as explained in Sect. 3. The surfaces of *m-D* coefficients derived using the matched radar Z and that with the bias corrections applied were similar, with the range of equally plausible b values differing, on average, by 6.4% after the corrections were made.

5.2 Accounting for mass contributions from larger particles

As discussed in Sect. 2.3.2, the Nevzorov probe is prone to larger particles ($D > 4$ mm) bouncing out of the collection cone resulting in potential TWC underestimations. Mass contents were derived from the PSDs using the modified BF95 ~~'s *m-D* relation~~ coefficients to identify time periods in which the contribution of mass from particles with $D > 4$ mm was likely greater than 20%. Of all 10 s PSDs used in this study, 20.9% had mass contributions from these larger particles exceeding 20% of the total mass. Figure 7 illustrates the similarity in the *(a,b)* surfaces generated using all coincident observations (red shading) and only those using observations with mass from larger particles contributing $\leq$ 20% of the total mass (blue shading) for the 23 May 2011 event. Regions of overlap between the two approaches only appear as ~~blue~~ purple shading. The sensitivity test shows that omitting observations where larger particles contribute fractionally more to the total mass yield an area of equally plausible (*a,b*) surfaces for the 23 May event differing, on average, by 1.4%~~and as such~~. As such, all coincident observations are used for this study irrespective of the fractional contributions of particles with $D > 4$ mm to the mass.

5.3 Environmental impact on *m-D* coefficients

Surfaces of equally plausible *m-D* coefficients in (*a,b*) phase space from all flight legs outlined in Table 1 are shown in Fig. 8. For each event, flight legs are grouped by the same environmental temperature with the different colors corresponding to the time periods given in each panel. These surfaces are influenced by how *TWC* and *Z* derived from the PSDs relate to observed *TWC* and *Z*, and by the variability of each within a flight leg. The observed trends in the (*a,b*) surfaces and how they are affected by *N(D)*, *TWC*, and *Z* are discussed further below.

To compare surfaces of equally plausible solutions between different environments and also between periods with the same temperature, the percent of overlap between any two flight legs is computed and shown as a matrix in Fig. 9. The percentage of overlap is determined by counting the number of (*a,b*) pairs contained in both equally plausible surfaces for the conditions listed in the row and column in the matrix and dividing by the number of (*a,b*) pairs in the surface for the condition listed in the row multiplied by 100%. There are two values in the matrix corresponding to each comparison between two flight legs, with differences between the two values resulting from dividing the area of the equally plausible surface from the corresponding column by that in the corresponding row in the matrix. Thus, it is possible for the percentage of overlap between two flight legs to be greater when normalized by an equally plausible surface that is smaller in area, and to be smaller when normalized by a larger equally plausible surface. It is worth noting that the percentage of overlap does not always follow an organized trend with respect to moving away from the gray diagonal line in the matrix as depicted in the top right corner of Fig. 9a. The lack of organized overlap values in some regions of the matrix could be influenced by the sensitivity in computing the overlap region over a fine resolution of (*a,b*) values within the domain described in Sect. 3, or perhaps could change in a more organized manner if there was a more statistically representative sample for these calculations to be made. Using the (*a,b*) surfaces from the -26.5 °C flight legs on 25 April (Fig. 8b) as an example, 62% of the (*a,b*) surface for the 11:05:20–11:14:45 UTC period (labeled -26.5 °C I; Fig. 9a) overlaps with the later -26.5 °C flight leg while 65% of the (*a,b*) surface for the 11:21:20–11:34:05 UTC period (labeled -26.5 °C II) overlaps with the earlier -26.5 °C flight leg. The difference occurs because there are 1132 (*a,b*) pairs in the surface for the 11:05:20–11:14:45 UTC period and 1077 (*a,b*) pairs in the surface for the 11:21:20–11:34:05 UTC period. Flight legs having the same temperature are ordered chronologically as in Fig. 8 and differentiated with a Roman numeral. Differences of the (*a,b*) surfaces between flight legs are further discussed below.

5.3.1 25 April case

While differences exist between the (*a,b*) surfaces for the near-constant temperature legs on 25 April (Fig. 9a), these surfaces have considerable overlap with each other for $a < 0.01$ g cm^{-b} and $b < 2.5$ (Figs. 8a-c). The -22 and -26.5 °C legs have similar sets of equally plausible solutions, with (*a,b*) surfaces overlapping between ~~44 and 90~~46 and 91% (Fig. 9a). Less agreement in the (*a,b*) surfaces is observed among the -35 °C flight legs, with the surfaces overlapping on average ~~23.4~~27.8% among the different combinations. The differences in the size of the surfaces is primarily influenced by the natural variability within cloud because ($\Delta\chi^2 = \chi^2_{min}$ > $\Delta\chi^2_1$ as shown in Sect. 3.) for 5 of the 7 legs and by the uncertainty due to measurement errors ($\Delta\chi^2 = \Delta\chi^2_2$) for the remaining legs. The areas of the (*a*,*b*) surfaces for the -22 and -26.5 °C legs were, on average, 37.5 31.2% smaller than the surfaces associated with the -35 °C environment (Figs. 8a-c). Three of the four -35 °C legs have surfaces larger than the -22 and -26.5 °C environments as the surface of equally plausible *m-D* coefficients extends beyond the maximum value *a* of 0.014 0.017 $\mathrm{g\ cm^{-b}}$ and *b* of 2.88 3.00 found for the -22 and -26.5 °C legs. To explain the variation of these (*a*,*b*) surfaces for the different temperatures, the distributions of microphysical quantities for the times corresponding to these surfaces were examined.

To examine the variability in hydrometeors, particle images and distributions of bulk microphysical properties were analyzed for each flight leg. Example particle images from the HVPS-3, which provide information on the size and habit of ice phase particles with $D > 1$ mm, are plotted in Fig. 10. The pictured particles represent a subset of those imaged for the time period given and were chosen at random in an attempt to obtain a representative sample of hydrometeors. Figure 11 shows the mean *N(D)* and cumulative mass distribution function *M(D)* using the modified BF95 relationship for each flight leg analyzed in this study. Figure 12 details the distribution of number concentration N_t, median mass diameter D_{mm}, and a metric for particle sphericity obtained from the PSDs derived from the 2D-C and HVPS-3 data at each 10 s coincident observation. The D_{mm} is derived using the modified BF95 coefficients to compare among the different flight legs. The whiskers and box edges are the same as in Fig. 6. Particle sphericity ζ (McFarquhar et al., 2005; Finlon et al., 2016) is defined by

$$\zeta = A^{1/2}/P, \tag{9}$$

where *A* is the cross-sectional area directly measured by the probe and *P* is the perimeter determined from the sum of all pixels within one diode width of the edge of the particle and the diode resolution. Finlon et al. (2016) described how higher ζ denotes more-circular particles. Sphericity values shown in Fig. 12 represent a mass-weighted mean of ζ for all particles using mass estimated from the modified BF95 relation within each 10 s observation. Figures 10and , 11, and 12 are ordered in the same manner as in Fig. 6, with instances of multiple legs having the same average temperature shown in chronological order.

As evidenced by the particle images and mean *N(D)* at T = -22 and -26.5 °C (Figs. 10a-c, 11a), the presence of aggregates exceeding 5 mm is more common compared to lower temperatures (Figs. 10d-g) where the ice crystals and aggregates appear to be skewed towards smaller sizes. Distributions of D_{mm} (Fig. 12b) and *TWC* (Fig. 6b) also indicate this trend, with a median D_{mm} for the 11:05:20–11:14:45 UTC (T = -26.5 °C) flight leg of 2.2 mm while the -35 °C periods have median D_{mm} ranging between 1.1 and 1.7 mm.

To illustrate that the range of equally plausible (*a*,*b*) coefficients are explained is sometimes explained more by the variability of cloud parameters than the uncertainty in measurement errors, the distributions of bulk microphysical variables, *TWC*, and *Z* are compared between the 11:05:20–11:14:45 UTC (T = -26.5 °C) and 10:03:05–10:08:45 UTC (T = -35 °C) periods. The -26.5 °C flight leg had ranges in N_t, D_{mm}, sphericity, *Z*, and *TWC* between the 25$^{\text{th}}$ and 75$^{\text{th}}$ percentiles (interquartile range hereafter) of 21.5 $\mathrm{L^{-1}}$, 1.3 mm, 0.04, 5.2 dBZ, and 0.73 $\mathrm{g\ m^{-3}}$, respectively, while the same variables for the -35 °C period had smaller interquartile ranges of 7.4 $\mathrm{L^{-1}}$, 0.1 mm, 0.02, 4.0 dBZ, and 0.17 $\mathrm{g\ m^{-3}}$ (Figs. 6a,b; 12a-c). The distribution of χ^2 in (*a*,*b*) phase space is expected to differ when the variability in *N(D)* throughout a flight leg is different between two periods since different *a* and *b* are likely to yield TWC_{SD} and Z_{SD} similar to the observed *TWC* and *Z*. Figure 13 illustrates the distribution of χ^2 for the two periods, with the outlined region representing χ^2 values that are ≤ 2 for comparison. The region containing $\chi^2 \leq 2$ is 90.8% smaller for the -26.5 °C flight leg compared to the -35 °C period and indicates that the TWC_{SD} and Z_{SD} derived from all possible *a* and *b* remain fairly consistent over the course of the -26.5 °C flight leg due to the smaller interquartile ranges in the *TWC*, *Z*, and bulk microphysical properties. As such, low χ^2 values are present over a larger range of *m-D* coefficients for the -35 °C leg.

Although the distribution of χ^2 is an important factor in determining the surface of equally plausible *m-D* coefficientsarea of an equally plausible surface, the $\Delta\chi^2$ confidence region, which is equal to χ^2_{min} for 15 of the 16 flight legs (Sect. 3), also influences the ($\Delta\chi^2_2$) for 4 (3) of the flight legs on this day, can also influence the area of (*a,b*) surfaces. While the allowable tolerance is a factor of 2 greater for the -26.5 °C leg, the equally plausible (*a,b*) surface is 3.4 times smaller compared to the -35 °C flight leg (Figs. 8b,c) because of the magnitude and distribution of χ^2 values in (*a,b*) phase space. Put another way, more χ^2 values considered within the (*a,b*) phase space are greater than the $\chi^2_{\mathrm{min}} + \Delta\chi^2$ criteria to be considered equally plausible solutions compared to the -35 °C leg.

5.3.2 20 May case

The wide range of temperatures sampled during the 20 May event was associated with a large variation in *Z* (Fig. 6c), with median values ranging between 12.5 dBZ (T = -23 °C) and 27.1 dBZ (T = -5.5 °C). Representative particle images (Fig. 14) highlight differences in particle size and habit between the higher temperature flight legs (T = -5.5 and -10.5 °C) and the lower temperature periods (T = -16 and -23 °C), with images and mean *N(D)* (Fig. 11b) from the -5.5 and -10.5 °C legs indicating a greater frequency of larger ice crystals and aggregates with $D \geq 2$ mm. A Mann-Whitney U test confirms that D_{mm} (Fig. 12e) and sphericity (Fig. 12f) between the higher and lower temperature environments are statistically different at the 99% confidence level, with notably larger and less spherical particles observed during the -5.5 and -10.5 °C flight legs. Further, median *Z* for the -5.5 and -10.5 °C periods (22.3–27.1 dBZ) are up to 30.7 times greater than for the -16 and -23 °C legs (12.2–12.5 dBZ) while the median *TWC* are up to 1.9 times (0.3 g m^{-3}) greater for the -5.5 and -10.5 °C legs. Thus, the difference in particle properties and bulk properties *TWC* and *Z* can be used to explain differences in (*a,b*) coefficients observed between the legs on this day.

Microphysical properties such as the effective density ρ_e of ice hydrometeors can impact *TWC* differently than they do *Z*. The ρ_e, defined here as the ratio of *TWC* derived assuming the modified BF95 relationship to the integrated volume of particles assuming an enclosed by an oblate spheroid with an aspect ratio of 0.6 (Hogan et al., 2012)(e.g., Hogan et al., 2012), is estimated to evaluate its influence on *TWC* and *Z*. Median ρ_e ranges between 0.05 and 0.08 g cm^{-3} for the -5.5 and -10.5 °C periods and between 0.18 and 0.21 g cm^{-3} for the -16 and -23 °C flight legs. These trends along with minimal riming evident from the 2D-C particle images suggest that particles are on average less compact for the higher temperature legs. Further, the presence of larger aggregates as suggested by greater values of D_{mm} (Fig. 12e), lower sphericity (Fig. 12f) and ρ_e, and the representative particle images from the HVPS-3 (Figs. 14a,b) are consistent with increasing *Z* when observed by longer wavelength radars (e.g., Giangrande et al., 2016).

Since differences in ρ_e appear to affect the *TWC* and *Z* on 20 May, the variability in *N(D)* is not the only factor influencing the equally plausible (*a,b*) surfaces depicted in Figs. 8d-g. Figure 9b illustrates that only the -16 and -23 °C legs have similar (*a,b*) surfaces, with ~~78~~85% of the (*a,b*) coefficients from the -16 °C leg overlapping with the -23 °C flight leg. Minimum values of *b* for the -5.5 and -10.5 °C flight legs, where less compact particles were observed, were ~~2.36 and 2.09~~1.84 and 1.66, respectively, while minimum *b* for the -16 and -23 °C legs were ~~1.74 and 1.51~~ 1.09 and 1.06 for similar *a* (Figs. 8d-g). Looking at the (*a,b*) surfaces another way, values of *a* for the -5.5 and -10.5 °C legs were as large as ~~0.016~~ 0.031 $\mathrm{g\ cm^{-b}}$ while *a* exceeds 0.05 $\mathrm{g\ cm^{-b}}$ for $b = 3$ during the -16 and -23 °C flight legs. ~~The~~ Although the $\Delta\chi^2$ confidence region is equal to $\Delta\chi^2_2$ for the 4 flight legs on this day and has $\Delta\chi^2$ values that are within 1% of each other, the distribution of χ^2 greatly influences the extent of these surfaces in (*a,b*) phase space ~~yields~~ with an area for the -5.5 and -10.5 °C flight legs that is on average ~~5.6~~ 2.9 times smaller than the the -16 and -23 °C periods. When considering the $m = aD^b$ relation whose size *D* and exponent *b* are held fixed, lower values of *a* as observed during the -5.5 and -10.5 °C legs suggest that particles on average have smaller *m* compared to the -16 and -23 °C legs and are consistent with smaller ρ_e observed for the -5.5 and -10.5 °C periods.

5.3.3 23 May case

The 23 May case was unique from the other two cases in that the bulk *Z* varied less between the different temperature environments (Fig. 6e), with median *Z* ranging only between 16.9 and 18.2 dBZ. Representative particle images (Fig. 15) in addition to the mean *N(D)* (Fig. 11c) and the cumulative *M(D)* (Fig. 11f) indicate that the sizes and shapes of ice hydrometeors are similar for all five flight legs. Additionally, distributions of D_{mm} (Fig. 12h) and sphericity (Fig. 12i), with median values of each varying by 0.4 mm and 0.04 respectively, ~~indicate that the sizes and shapes of ice hydrometeors are also similar for all five flight legs~~further support this similarity in cloud properties between the different environments. Equally plausible (*a,b*) surfaces were also similar irrespective of temperature (Figs. 8h,i), with the four flight legs after the 21:49:55–21:55:15 UTC period having surfaces that overlap on average ~~56.1~~62.1% among the different combinations (Fig. 9c). The 21:49:55–21:55:15 UTC leg is the only period ~~where its (~~on this day where the $\Delta\chi^2$ confidence region is determined by the natural variability in the cloud (χ^2_{min}) rather than the uncertainty due to measurement errors ($\Delta\chi^2_2$). As such, the (*a,b*) surface for this period has minimal overlap with the other equally plausible surfaces. Closer examination of the bulk *TWC* (Fig. 6f) indicates that values at the fifth percentile for the 21:49:55–21:55:15 UTC period are 65.2% less than the remaining flight legs, which impacts the distribution of χ^2 values and the (*a,b*) values that are within the $\chi^2_{\text{min}} + \Delta\chi^2$ threshold.

Although surfaces of equally plausible solutions trend larger in area for lower temperature environments on 25 April and 20 May, the area of (*a,b*) surfaces among the five flight legs on 23 May are on average ~~6.8 (6.4~~2.2 (3.8) times smaller compared to the 25 April (20 May) event. To examine how the distribution of χ^2 in (*a,b*) phase space is affected by differences in the variability of *TWC* and *Z* throughout a flight leg, the 14:16:30–14:32:15 UTC period on 20 May and the 21:49:55–21:55:15 UTC period on 23 May are compared because of their similar temperature and $\chi^2_{\text{min}} + \Delta\chi^2$ threshold used to determine the (*a,b*) surfaces. Figure 16 illustrates the distribution of χ^2 for the two periods, with the outlined region representing χ^2 values that are ≤ 1 for the purpose of comparison. The region containing $\chi^2 \leq 1$ is 88.2% smaller for the 23 May flight leg compared to the 20 May period, and highlights how different *a* and *b* can yield a χ^2 value that is within the given tolerance based on differences in the observed *TWC* and *Z* distributions. When bulk *TWC* and *Z* are compared against the 25 April (20 May) events, the median *Z* from flight legs on 23 May is on average 34.4% (25.9%) lower while the median *TWC* is 90.3% (43.9%) greater. As mentioned in Sect. 4, the sampling strategy on 23 May was different from the stratiform clouds observed with the previous two events in that measurements were primarily made in the anvil region of supercell thunderstorms. Previous studies (e.g., Heymsfield et al., 2007) noted that the prefactor *a* had less of a temperature dependence within anvil cirrus clouds, consistent with trends in *a* for the 23 May flight legs.

6 Conclusions

This paper presented a novel approach to characterize the variability of mass-Dimension (*m-D*) coefficients characterizing particle size distributions (PSDs) during the Mid-latitude Continental Convective Clouds Experiment (MC3E). The technique outlined here extends the approach of McFarquhar et al. (2015), who derived a volume of equally realizable solutions in the phase space of gamma fit parameter coefficients to characterize PSDs. Ground-based radar measurements of reflectivity *Z* from the Vance Air Force Base, OK radar were matched to the location of the Cessna Citation II aircraft where total water content (*TWC*) measurements from the Nevzorov probe were made and PSDs were derived from optical array probe data. These collocated datasets permitted use of a χ^2 minimization technique where all χ^2 within a tolerance $\Delta\chi^2$ of the minimum χ^2 were considered equally plausible solutions to the $m = aD^b$ relationship for a flight leg of similar temperature. The tolerance was determined by considering uncertainties due to natural variability of cloud conditions for a particular environment~~and~~, the statistical sampling of particles from the PSDs, and uncertainties in the measurements themselves.

The key findings of the paper are as follows:

1. The distribution of χ^2 values in (*a*,*b*) phase space shows that the *a* and *b* parameters are highly correlated, as expected. The ~~distribution of how the (*a*,*b*) parameters vary for a given~~ degree to which these χ^2 values vary throughout a flight leg is influenced by how the PSDs, *TWC* from the Nevzorov probe, and *Z* from radar vary within a flight leg of similar temperature. Flight legs that have little variability in the microphysical properties and an allowable tolerance equal to the minimum χ^2 in (*a*,*b*) phase space, such as the 10:03:05–10:08:45 UTC period on 25 April, occupy a surface area in (*a*,*b*) phase space that is up to ~~10.9~~ 8.7 times larger than flight legs where microphysical properties vary more, such as the 11:05:20–11:14:45 UTC leg on the same day.

2. Surfaces of equally plausible solutions appear dependent on temperature for the 25 April and 20 May events. The range of plausible *a* and *b* coefficients is larger for flight legs of lower temperature, and 80% of the surfaces compared between the lowest and highest temperature for each day overlap by less than 50%.

3. Cases with little dependence of the surfaces of equally plausible solutions on temperature, like the flight legs analyzed on 23 May, can be explained in terms of the regions of cloud sampled and the types of ice hydrometeors observed. A mean overlap of ~~56.1~~62.1% between four of the five (*a*,*b*) surfaces on that day is consistent with previous studies (e.g., Heymsfield et al., 2007) that note little dependence in the *a* coefficient with temperature in anvil cirrus clouds.

4. The minimum χ^2 in (*a*,*b*) phase space determines the allowable tolerance $\Delta\chi^2$ for 15 5 of the 16 flight legs when determining the set of equally plausible *a* and *b* coefficients, meaning whereas the combined uncertainty due to measurement error from the OAPs, Nevzorov *TWC* probe, and radar determines the $\Delta\chi^2$ for the remaining 11 flight legs. This means that the uncertainty in the *m*-*D* coefficients is primarily driven by the driven by uncertainties in the measurements the majority of the time, with the natural parameter variability over a flight leg rather than the uncertainty in the PSDs due to uncertainties in sampling statisticsa driving factor for 31% of the flight legs observed. Thus, efforts to reduce measurement errors could reduce the uncertainty in derived (*a*,*b*) coefficients.

5. The covariability of *a* and *b* permit possible solutions of $b > 3$ for the ranges of particle sizes observed in 6 7 of the 16 flight legs analyzed. For these flight legs this covariability means that *Z* derived from *a* and *b* and the PSDs is still within 82.4% of the mean matched radar *Z*, which is marginally greater than the 50.5% difference when *b* is not greater than 3.

6. Flight legs where the cloud particles have lower effective density ρ_e, such as the -5.5 and -10.5 °C flight legs on 20 May, yield minimum *b* values in (*a*,*b*) phase space as much as 0.85 0.78 larger than clouds with a higher ρ_e like the -16 and -23 °C legs on the same day. These differences can be explained by the different impacts of ρ_e on *TWC* compared to *Z*.

A key finding of this study is that a range of *a* and *b* coefficients should be considered as equally plausible for a given environment due to the natural variability of cloud conditions and measurement uncertainties, even within a similar temperature range. This variability results in a large range of *a* and *b* as equally plausible solutions (as indicated in this study), and explains could explain the range in *m*-*D* coefficients determined in past studies (Fig. 1) where *a* coefficients can vary by 3 orders of magnitude and *b* coefficients between 1 and 3 for measurements made in similar environmental conditions. The technique used in this study provides insight into how equally plausible *m*-*D* coefficients can arise because the dependence of derived microphysical parameters on environmental conditions is generally sometimes more important than measurement uncertainties based on the instruments used to collect the data, but is not always the case. Further, it is shown that the dependence of the (*a*,*b*) coefficients on temperature is still notable even when considering the ranges of equally plausible solutions. Future studies should further ascertain the extent to which the dependence of (*a*,*b*) on other environmental parameters is robust enough to be distinguished from the natural variability of the surface or its variability due to measurement errors.

While representing *m*-*D* coefficients as a range of equally plausible solutions may address shortcomings of microphysical parameterization schemes and remote sensing retrievals that employ a single *m*-*D* relationship for a given ice species or environment, caution should be taken if the results presented here are applied to ranges of particle size or environments outside of those sampled (e.g., ones with different observed habits or various degrees of riming)to develop this parameterization. . The results presented here illustrate that similar *TWC* and *Z* can be obtained regardless of the *a* and *b* values chosen, with coefficients randomly selected from a surface of solutions allowing one to represent how the uncertainty in (*a*,*b*) impacts any derived quantity. Thus, the large variability in derived (*a*,*b*) for an equally plausible surface does not necessarily indicate there is a large uncertainty in quantities derived using the *a* and *b* coefficients. Future work should assess how the representation of modeled processes and retrieved quantities are influenced by the variability in *a* and *b* coefficients as well as which environmental drivers and cloud microphysical properties influence the size of derived surfaces of equally plausible solutions, and the extent to which measurement errors need to be reduced to better refine these surfaces. The approach presented in this study can be applied to additional studies that make use of collocated radar and microphysical measurements in other cloud and meteorological environments, and improve the statistical robustness of plausible *m-D* parameters for given environmental conditions. Such studies may help to further understand how surfaces of equally plausible (*a,b*) solutions are affected by different environments and the variability of cloud conditions therein, as well as the dependence of these solutions as a function of other cloud or environmental properties.

Code and data availability. The radar (doi: 10.5067/MC3E/NEXRAD/DATA202) and OAP (doi: 10.5067/GPMGV/MC3E/MULTIPLE/DATA201) data used in this study are found on the NASA GHRC MC3E data archive. The software packages used to match the radar data to the aircraft's location (https://github.com/swnesbitt/AWOT) and to process the OAP data (doi: 10.5281/zenodo.1285969) are openly available as GitHub repositories. The data containing matched radar and microphysical properties (doi: 10.13012/B2IDB-6396968_V1) used in this study are archived and available online.

Appendix A: List of variables and their descriptions

a	Prefactor component in mass-Dimension relationship
A	Particle cross-sectional area
b	Exponent component in mass-Dimension relationship
χ^2	Chi-square statistic for each (a,b) over a flight leg
$\chi^2{}_{\mathrm{min}}$	Lowest χ^2 value in (a,b) phase space for a flight leg
$\Delta\chi_1^2$	~~Uncertainty~~ Threshold determined from uncertainty in the particle size distribution due to sampling statistics
$\Delta\chi_2^2$	Threshold determined from combined uncertainty due to measurement errors
$\Delta\chi^2$	Maximum value ~~between~~ of $\chi^2{}_{\mathrm{min}}$ ~~and~~ , $\Delta\chi_1^2$, or $\Delta\chi_2^2$
D	Particle maximum dimension
D_{mm}	Median mass diameter
IWC	Ice water content
K_{DP}	Specific differential phase
$\lvert K_{\mathrm{ice}}\rvert^2$	Dielectric constant for ice
$\lvert K_w\rvert^2$	Dielectric constant for water
$M(D)$	Mass distribution function
$N(D)$	Number distribution function
N_t	~~Number~~ Total number concentration
P	Particle perimeter
ρ_e	Effective density
SDP	Sigma differential phase
T	Environmental temperature
TWC	Total water content measurement
TWC_{diff}	Measure of normalized ~~Normalized~~ difference between the Nevzorov *TWC* and that derived from the *N(D)* for a given (a,b) defined by Eq. (3)
TWC_{SD}	*TWC* derived from the *N(D)* for a given (a,b)
ζ	Particle sphericity
Z	Radar reflectivity factor
$Z_c(D)$	Cumulative reflectivity distribution function up to size D'
$Z(D)$	Reflectivity distribution function
Z_{diff}	Measure of normalized ~~Normalized~~ difference between the radar Z and that derived from the *N(D)* for a given (a,b) defined by Eq. (4)
Z_{DR}	Differential reflectivity
Z_{SD}	Z derived from the *N(D)* for a given (a,b)
Z_t	Derived total reflectivity from the mean *N(D)* for a given (a,b)

Author contributions. JF prepared the manuscript and performed all the calculations with contributions from all co-authors. GM provided the idea and formulated the framework for the study, SN provided the framework for matching radar gates to an aircraft's position~~.~~, WW processed particle data from the optical array probes~~.~~, PZ conducted the radar bias calculations used in this study~~.~~, and RR and HM provided feedback on the ideas and calculations presented.

Competing interests. The authors declare that they have no conflict of interest.

Acknowledgements. This research was supported by the US Department of Energy grants DE-SC0014065 and DE-SC0016476 (through UCAR subcontract SUBAWD000397)~~and~~ , by the NASA Precipitation Measurement Missions grant NNX16AD80G, and by the National Science Foundation grant AGS-1247404. We thank all participants of MC3E for collecting the data used in this study.

References

Barnes, S. L.: A Technique for Maximizing Details in Numerical Weather Map Analysis, Journal of Applied Meteorology, 3, 396–409, https://doi.org/10.1175/1520-0450(1964)003<0396:ATFMDI>2.0.CO;2, http://journals.ametsoc.org/doi/abs/10.1175/1520-0450%281964%29003%3C0396%3AATFMDI%3E2.0.CO%3B2#.WKz-Eb_dSWU.mendeley, 1964.

Baumgardner, D. and Korolev, A.: Airspeed Corrections for Optical Array Probe Sample Volumes, Journal of Atmospheric and Oceanic Technology, 14, 1224–1229, https://doi.org/10.1175/1520-0426(1997)014<1224:ACFOAP>2.0.CO;2, http://journals.ametsoc.org/doi/full/10.1175/1520-0426%281997%29014%3C1224%3AACFOAP%3E2.0.CO%3B2#.WKs_amkB-pI.mendeley, 1997.

Bringi, V. N. and Chandrasekar, V.: Polarimetric Doppler Weather Radar: Principles and Applications, Cambridge University Press, http://books.google.com/books?id=KvJvfP9t5Y8C, 2001.

Bringi, V. N., Chandrasekar, V., Balakrishnan, N., and Zrnić, D. S.: An Examination of Propagation Effects in Rainfall on Radar Measurements at Microwave Frequencies, Journal of Atmospheric and Oceanic Technology, 7, 829–840, https://doi.org/10.1175/1520-0426(1990)007<0829:AEOPEI>2.0.CO;2, http://dx.doi.org/10.1175/1520-0426(1990)007%3C0829:AEOPEI%3E2.0.CO2, 1990.

Brown, P. R. A. and Francis, P. N.: Improved Measurements of the Ice Water Content in Cirrus Using a Total-Water Probe, Journal of Atmospheric and Oceanic Technology, 12, 410–414, https://doi.org/10.1175/1520-0426(1995)012<0410:IMOTIW>2.0.CO;2, http://dx.doi.org/10.1175/1520-0426(1995)012%3C0410:IMOTIW%3E2.0.CO%5Cn2, 1995.

Cazenave, F., Gosset, M., Kacou, M., Alcoba, M., Fontaine, E., Duroure, C., and Dolan, B.: Characterization of Hydrometeors in Sahelian Convective Systems with an X-Band Radar and Comparison with In Situ Measurements. Part I: Sensitivity of Polarimetric Radar Particle Identification Retrieval and Case Study Evaluation, Journal of Applied Meteorology and Climatology, 55, 231–249, https://doi.org/10.1175/JAMC-D-15-0013.1, http://dx.doi.org/10.1175/JAMC-D-15-0013.1, 2016.

Cotton, R. J., Field, P. R., Ulanowski, Z., Kaye, P. H., Hirst, E., Greenaway, R. S., Crawford, I., Crosier, J., and Dorsey, J.: The effective density of small ice particles obtained from in situ aircraft observations of mid-latitude cirrus, Quarterly Journal of the Royal Meteorological Society, 139, 1923–1934, https://doi.org/10.1002/qj.2058, http://onlinelibrary.wiley.com/doi/10.1002/qj.2058/full, 2013.

Delanoë, J. and Hogan, R. J.: Combined CloudSat-CALIPSO-MODIS retrievals of the properties of ice clouds, Journal of Geophysical Research, 115, D00H29–D00H29, https://doi.org/10.1029/2009JD012346, http://doi.wiley.com/10.1029/2009JD012346, 2010.

Erfani, E. and Mitchell, D. L.: Developing and bounding ice particle mass- and area-dimension expressions for use in atmospheric models and remote sensing, Atmospheric Chemistry and Physics, 16, 4379–4400, https://doi.org/10.5194/acp-16-4379-2016, http://www.atmos-chem-phys.net/16/4379/2016/, 2016.

Field, P. R.: Aircraft Observations of Ice Crystal Evolution in an Altostratus Cloud, Journal of the Atmospheric Sciences, 56, 1925–1941, https://doi.org/10.1175/1520-0469(1999)056<1925:AOOICE>2.0.CO;2, http://dx.doi.org/10.1175/1520-0469(1999)056%3C1925:AOOICE%3E2.0.CO, 1999.

Field, P. R., Wood, R., Brown, P. R. A., Kaye, P. H., Hirst, E., Greenaway, R., and Smith, J. A.: Ice Particle Interarrival Times Measured with a Fast FSSP, Journal of Atmospheric and Oceanic Technology, 20, 249–261, https://doi.org/10.1175/1520-0426(2003)020<0249:IPITMW>2.0.CO;2, http://journals.ametsoc.org/doi/abs/10.1175/1520-0426%282003%29020%3C0249%3AIPITMW%3E2.0.CO%3B2#.WKtvq7rTK_o.mendeley, 2003.

Field, P. R., Heymsfield, A. J., and Bansemer, A.: Shattering and Particle Interarrival Times Measured by Optical Array Probes in Ice Clouds, Journal of Atmospheric and Oceanic Technology, 23, 1357–1371, https://doi.org/10.1175/JTECH1922.1, http://dx.doi.org/10.1175/JTECH1922.1, 2006.

Finlon, J. A., McFarquhar, G. M., Rauber, R. M., Plummer, D. M., Jewett, B. F., Leon, D., and Knupp, K. R.: A Comparison of X-Band Polarization Parameters with In Situ Microphysical Measurements in the Comma Head of Two Winter Cyclones, Journal of Applied Meteorology and Climatology, 55, 2549–2574, https://doi.org/10.1175/JAMC-D-16-0059.1, https://journals.ametsoc.org/doi/full/10.1175/JAMC-D-16-0059.1, 2016.

Fontaine, E., Schwarzenboeck, A., Delanoë, J., Wobrock, W., Leroy, D., Dupuy, R., Gourbeyre, C., and Protat, A.: Constraining mass–diameter relations from hydrometeor images and cloud radar reflectivities in tropical continental and oceanic convective anvils, Atmospheric Chemistry and Physics, 14, 11 367–11 392, https://doi.org/10.5194/acp-14-11367-2014, http://www.atmos-chem-phys.net/14/11367/2014/acp-14-11367-2014.html, 2014.

Giangrande, S. E., Toto, T., Bansemer, A., Kumjian, M. R., Mishra, S., and Ryzhkov, A. V.: Insights into riming and aggregation processes as revealed by aircraft, radar, and disdrometer observations for a 27 April 2011 widespread precipitation event, Journal of Geophysical Research: Atmospheres, 121, 5846–5863, https://doi.org/10.1002/2015JD024537, https://agupubs.onlinelibrary.wiley.com/doi/abs/10.1002/2015JD024537, 2016.

Hallett, J.: Handbook of Weather, Climate, and Water, John Wiley & Sons, Inc., Hoboken, NJ, USA, https://doi.org/10.1002/0471721603, http://onlinelibrary.wiley.com/resolve/doi?DOI=10.1002%2F0471721603.ch35#.WKnnG2yKXto.mendeley, 2003.

Helmus, J. and Collis, S.: The Python ARM Radar Toolkit (Py-ART), a Library for Working with Weather Radar Data in the Python Programming Language, Journal of Open Research Software, 4, https://doi.org/10.5334/jors.119, http://openresearchsoftware.metajnl.com/articles/10.5334/jors.119/, 2016.

Heymsfield, A.: Ice Crystal Terminal Velocities, Journal of the Atmospheric Sciences, 29, 1348–1357, https://doi.org/10.1175/1520-0469(1972)029<1348:ICTV>2.0.CO;2, http://journals.ametsoc.org/doi/abs/10.1175/1520-0469(1972)029%3C1348:ICTV%3E2.0.CO%3B2%5Cnhttp://journals.ametsoc.org/doi/pdf/10.1175/1520-0469(1972)029%3C1348:ICTV%3E2.0.CO%3B2, 1972.

Heymsfield, A. J. and Baumgardner, D.: Summary of a workshop on processing 2–D probe data, Bulletin of the American Meteorological Society, 66, 437–440, 1985.

Heymsfield, A. J., Lewis, S., Bansemer, A., Iaquinta, J., Miloshevich, L. M., Kajikawa, M., Twohy, C., and Poellot, M. R.: A General Approach for Deriving the Properties of Cirrus and Stratiform Ice Cloud Particles, Journal of the Atmospheric Sciences, 59, 3–29, https://doi.org/10.1175/1520-0469(2002)059<0003:AGAFDT>2.0.CO;2, http://dx.doi.org/10.1175/1520-0469(2002)059%3C0003:AGAFDT%3E2.0.CO, 2002.

Heymsfield, A. J., Bansemer, A., and Twohy, C. H.: Refinements to Ice Particle Mass Dimensional and Terminal Velocity Relationships for Ice Clouds. Part I: Temperature Dependence, Journal of the Atmospheric Sciences, 64, 1047–1067, https://doi.org/10.1175/JAS3890.1, http://dx.doi.org/10.1175/JAS3890.1, 2007.

Heymsfield, A. J., Schmitt, C., Bansemer, A., and Twohy, C. H.: Improved Representation of Ice Particle Masses Based on Observations in Natural Clouds, Journal of the Atmospheric Sciences, 67, 3303–3318, https://doi.org/10.1175/2010JAS3507.1, http://dx.doi.org/10.1175/2010JAS3507.1, 2010.

Heymsfield, A. J., Field, P. R., Bailey, M., Rogers, D., Stith, J., Twohy, C., Wang, Z., and Haimov, S.: Ice in Clouds Experiment—Layer Clouds. Part I: Ice Growth Rates Derived from Lenticular Wave Cloud Penetrations, Journal of the Atmospheric Sciences, 68, 2628–2654, https://doi.org/10.1175/JAS-D-11-025.1, https://journals.ametsoc.org/doi/full/10.1175/JAS-D-11-025.1, 2011.

Heymsfield, A. J., Schmitt, C., and Bansemer, A.: Ice Cloud Particle Size Distributions and Pressure-Dependent Terminal Velocities from In Situ Observations at Temperatures from 0° to -86°C, Journal of the Atmospheric Sciences, 70, 4123–4154, https://doi.org/10.1175/JAS-D-12-0124.1, http://dx.doi.org/10.1175/JAS-D-12-0124.1, 2013.

Hogan, R. J., Illingworth, A. J., and Sauvageot, H.: Measuring crystal size in cirrus using 35- and 94-GHz radars, Journal of Atmospheric and Oceanic Technology, 17, 27–37, https://doi.org/10.1175/1520-0426(2000)017<0027:MCSICU>2.0.CO;2, 2000.

Hogan, R. J., Mittermaier, M. P., and Illingworth, A. J.: The Retrieval of Ice Water Content from Radar Reflectivity Factor and Temperature and Its Use in Evaluating a Mesoscale Model, Journal of Applied Meteorology and Climatology, 45, 301–317, https://doi.org/10.1175/JAM2340.1, http://dx.doi.org/10.1175/JAM2340.1, 2006.

Hogan, R. J., Tian, L., Brown, P. R. a., Westbrook, C. D., Heymsfield, A. J., and Eastment, J. D.: Radar Scattering from Ice Aggregates Using the Horizontally Aligned Oblate Spheroid Approximation, Journal of Applied Meteorology and Climatology, 51, 655–671, https://doi.org/10.1175/JAMC-D-11-074.1, http://journals.ametsoc.org/doi/abs/10.1175/JAMC-D-11-074.1, 2012.

Ice, R. L., Richardson, L. M., Daniel, A. E., Free, A. D., Macemon, R. W., Krause, J. C., Secrest, G., Lee, R. R., Melnikov, V. M., and Hubbert, J. C.: Monitoring the Performance of the Polarimetric WSR-88D–Calibration and Sensitivity, in: 33rd Conference on Environmental Information Processing Technologies, American Meteorological Society, 2017.

Jackson, R. C., McFarquhar, G. M., Stith, J., Beals, M., Shaw, R. A., Jensen, J., Fugal, J., and Korolev, A.: An Assessment of the Impact of Antishattering Tips and Artifact Removal Techniques on Cloud Ice Size Distributions Measured by the 2D Cloud Probe, Journal of Atmospheric and Oceanic Technology, 31, 2567–2590, https://doi.org/10.1175/JTECH-D-13-00239.1, http://dx.doi.org/10.1175/JTECH-D-13-00239.1, 2014.

Jensen, M. P., Giangrande, S. E., and Kollias, P.: The Mid-latitude Continental Convective Clouds Experiment (MC3E) Final Campaign Report, pp. 1–13, https://www.arm.gov/publications/programdocs/doe-sc-arm-14-012.pdf, 2014.

Jensen, M. P., Petersen, W. A., Bansemer, A., Bharadwaj, N., Carey, L. D., Cecil, D. J., Collis, S. M., Del Genio, A. D., Dolan, B., Gerlach, J., Giangrande, S. E., Heymsfield, A., Heymsfield, G., Kollias, P., Lang, T. J., Nesbitt, S. W., Neumann, A., Poellot, M., Rutledge, S. A., Schwaller, M., Tokay, A., Williams, C. R., Wolff, D. B., Xie, S., Zipser, E. J., Jensen, M. P., Petersen, W. A., Bansemer, A., Bharadwaj, N., Carey, L. D., Cecil, D. J., Collis, S. M., Genio, A. D. D., Dolan, B., Gerlach, J., Giangrande, S. E., Heymsfield, A., Heymsfield, G., Kollias, P., Lang, T. J., Nesbitt, S. W., Neumann, A., Poellot, M., Rutledge, S. A., Schwaller, M., Tokay, A., Williams, C. R., Wolff, D. B., Xie, S., and Zipser, E. J.: The Midlatitude Continental Convective Clouds Experiment (MC3E), Bulletin of the American Meteorological Society, 97, 1667–1686, https://doi.org/10.1175/BAMS-D-14-00228.1, http://journals.ametsoc.org/doi/10.1175/BAMS-D-14-00228.1, 2016.

Korolev, A. and Field, P. R.: Assessment of the performance of the inter-arrival time algorithm to identify ice shattering artifacts in cloud particle probe measurements, Atmospheric Measurement Techniques, 8, 761–777, https://doi.org/10.5194/amt-8-761-2015, http://www.atmos-meas-tech.net/8/761/2015/, 2015.

Korolev, A., Emery, E., and Creelman, K.: Modification and Tests of Particle Probe Tips to Mitigate Effects of Ice Shattering, Journal of Atmospheric and Oceanic Technology, 30, 690–708, https://doi.org/10.1175/JTECH-D-12-00142.1, http://journals.ametsoc.org/doi/abs/10.1175/JTECH-D-12-00142.1, 2013a.

Korolev, A., Strapp, J. W., Isaac, G. A., and Emery, E.: Improved Airborne Hot-Wire Measurements of Ice Water Content in Clouds, Journal of Atmospheric and Oceanic Technology, 30, 2121–2131, https://doi.org/10.1175/JTECH-D-13-00007.1, http://journals.ametsoc.org/doi/full/10.1175/JTECH-D-13-00007.1#.WKtZQDVS8co.mendeley, 2013b.

Korolev, A. V., Strapp, J. W., Isaac, G. A., and Nevzorov, A. N.: The Nevzorov Airborne Hot-Wire LWC–TWC Probe: Principle of Operation and Performance Characteristics, Journal of Atmospheric and Oceanic Technology, 15, 1495–1510, https://doi.org/10.1175/1520-0426(1998)015<1495:TNAHWL>2.0.CO;2, https://journals.ametsoc.org/doi/abs/10.1175/1520-0426%281998%29015%3C1495%3ATNAHWL%3E2.0.CO%3B2, 1998.

Korolev, A. V., Emery, E. F., Strapp, J. W., Cober, S. G., Isaac, G. A., Wasey, M., and Marcotte, D.: Small Ice Particles in Tropospheric Clouds: Fact or Artifact? Airborne Icing Instrumentation Evaluation Experiment, Bulletin of the American Meteorological Society, 92, 967–973, https://doi.org/10.1175/2010BAMS3141.1, http://dx.doi.org/10.1175/2010BAMS3141.1, 2011.

Krajewski, W. F. and Ciach, G. J.: Towards Probabilistic Quantitative Precipitation WSR88D Algorithms: Preliminary Studies and Problem Formulation, Tech. Rep. DG133W-02-CN-0089, NOAA/NWS, http://www.nws.noaa.gov/oh/hrl/papers/wsr88d/PQPE-Year1-FinalReport_v2.pdf, 2003.

Lawson, R. P., Woods, S., and Morrison, H.: The Microphysics of Ice and Precipitation Development in Tropical Cumulus Clouds, Journal of the Atmospheric Sciences, 72, 2429–2445, https://doi.org/10.1175/JAS-D-14-0274.1, https://journals.ametsoc.org/doi/10.1175/JAS-D-14-0274.1, 2015.

Lemke, H. M. and Quante, M.: Backscatter characteristics of nonspherical ice crystals: Assessing the potential of polarimetric radar measurements, Journal of Geophysical Research: Atmospheres, 104, 31 739–31 751, https://doi.org/10.1029/1999JD900490, http://doi.wiley.com/10.1029/1999JD900490, 1999.

Leroy, D., Fontaine, E., Schwarzenboeck, A., and Strapp, J. W.: Ice Crystal Sizes in High Ice Water Content Clouds. Part I: On the Computation of Median Mass Diameter from In Situ Measurements, Journal of Atmospheric and Oceanic Technology, 33, 2461–2476, https://doi.org/10.1175/JTECH-D-15-0151.1, http://journals.ametsoc.org/doi/10.1175/JTECH-D-15-0151.1, 2016.

Liu, G. and Curry, J. a.: Determination of Ice Water Path and Mass Median Particle Size Using Multichannel Microwave Measurements, Journal of Applied Meteorology, 39, 1318–1329, https://doi.org/10.1175/1520-0450(2000)039<1318:DOIWPA>2.0.CO;2, 2000.

Locatelli, J. D. and Hobbs, P. V.: Fall speeds and masses of solid precipitation particles, Journal of Geophysical Research, 79, 2185–2197, https://doi.org/10.1029/JC079i015p02185, http://onlinelibrary.wiley.com/doi/10.1029/JC079i015p02185/abstract%5Cnhttp://onlinelibrary.wiley.com/store/10.1029/JC079i015p02185/asset/jgr14894.pdf?v=1&t=i1h8td42&s=bea840a363a286e28adb6368e5b7ef447d7e173f, 1974.

Maahn, M., Löhnert, U., Kollias, P., Jackson, R. C., and McFarquhar, G. M.: Developing and Evaluating Ice Cloud Parameterizations for Forward Modeling of Radar Moments Using in situ Aircraft Observations, Journal of Atmospheric and Oceanic Technology, 32, 880–903, https://doi.org/10.1175/JTECH-D-14-00112.1, http://dx.doi.org/10.1175/JTECH-D-14-00112.1, 2015.

Magono, C. and Nakamura, T.: Aerodynamic Studies of Falling Snowflakes, Journal of the Meteorological Society of Japan, 43, 139–147, 1965.

Maneewongvatana, S. and Mount, D. M.: It's okay to be skinny, if your friends are fat, in: 4th Annual CGC Workshop on Computational Geometry, 1999.

Mascio, J., Xu, Z., and Mace, G. G.: The Mass-Dimensional Properties of Cirrus Clouds During TC4, Journal of Geophysical Research: Atmospheres, 122, 10,402–10,417, https://doi.org/10.1002/2017JD026787, http://doi.wiley.com/10.1002/2017JD026787, 2017.

Matrosov, S. Y.: Modeling Backscatter Properties of Snowfall at Millimeter Wavelengths, Journal of the Atmospheric Sciences, 64, 1727–1736, https://doi.org/10.1175/JAS3904.1, http://journals.ametsoc.org/doi/full/10.1175/JAS3904.1%5Cnhttp://journals.ametsoc.org/doi/pdf/10.1175/JAS3904.1, 2007.

Matrosov, S. Y.: Assessment of Radar Signal Attenuation Caused by the Melting Hydrometeor Layer, IEEE Transactions on Geoscience and Remote Sensing, 46, 1039–1047, https://doi.org/10.1109/TGRS.2008.915757, 2008.

McCumber, M., Tao, W.-K., Simpson, J., Penc, R., Soong, S.-T., McCumber, M., Tao, W.-K., Simpson, J., Penc, R., and Soong, S.-T.: Comparison of Ice-Phase Microphysical Parameterization Schemes Using Numerical Simulations of Tropical Convection, Journal of Applied

Meteorology, 30, 985–1004, https://doi.org/10.1175/1520-0450-30.7.985, http://journals.ametsoc.org/doi/abs/10.1175/1520-0450-30.7.985, 1991.

McFarquhar, G. M. and Heymsfield, A. J.: Microphysical Characteristics of Three Anvils Sampled during the Central Equatorial Pacific Experiment, Journal of the Atmospheric Sciences, 53, 2401–2423, https://doi.org/10.1175/1520-0469(1996)053<2401:MCOTAS>2.0.CO;2, http://dx.doi.org/10.1175/1520-0469(1996)053%3C2401:MCOTAS%3E2.0.CO, 1996.

McFarquhar, G. M., Timlin, M. S., Nousiainen, T., and Yang, P.: A New Representation of the Single-Scattering Properties for Mid-latitude Clouds and its Impacts, in: Fifteenth ARM Science Team Meeting Proceedings, http://www.arm.gov/publications/proceedings/conf15/extended_abs/mcfarquhar_gm2.pdf?id=26, 2005.

McFarquhar, G. M., Timlin, M. S., Rauber, R. M., Jewett, B. F., Grim, J. A., and Jorgensen, D. P.: Vertical Variability of Cloud Hydrometeors in the Stratiform Region of Mesoscale Convective Systems and Bow Echoes, Monthly Weather Review, 135, 3405–3428, https://doi.org/10.1175/MWR3444.1, http://dx.doi.org/10.1175/MWR3444.1, 2007a.

McFarquhar, G. M., Zhang, G., Poellot, M. R., Kok, G. L., McCoy, R., Tooman, T., Fridlind, A., and Heymsfield, A. J.: Ice properties of single-layer stratocumulus during the Mixed-Phase Arctic Cloud Experiment: 1. Observations, Journal of Geophysical Research: Atmospheres, 112, 1–19, https://doi.org/10.1029/2007JD008633, 2007b.

McFarquhar, G. M., Hsieh, T.-L., Freer, M., Mascio, J., and Jewett, B. F.: The Characterization of Ice Hydrometeor Gamma Size Distributions as Volumes in N_0-μ-λ Phase Space: Implications for Microphysical Process Modeling, Journal of the Atmospheric Sciences, 72, 892–909, https://doi.org/10.1175/JAS-D-14-0011.1, http://dx.doi.org/10.1175/JAS-D-14-0011.1, 2015.

McFarquhar, G. M., Baumgardner, D., Bansemer, A., Abel, S. J., Crosier, J., French, J., Rosenberg, P., Korolev, A., Schwarzoenboeck, A., Leroy, D., Um, J., Wu, W., Heymsfield, A. J., Twohy, C., Detwiler, A., Field, P., Neumann, A., Cotton, R., Axisa, D., Dong, J., McFarquhar, G. M., Baumgardner, D., Bansemer, A., Abel, S. J., Crosier, J., French, J., Rosenberg, P., Korolev, A., Schwarzoenboeck, A., Leroy, D., Um, J., Wu, W., Heymsfield, A. J., Twohy, C., Detwiler, A., Field, P., Neumann, A., Cotton, R., Axisa, D., and Dong, J.: Processing of Ice Cloud In Situ Data Collected by Bulk Water, Scattering, and Imaging Probes: Fundamentals, Uncertainties, and Efforts toward Consistency, Meteorological Monographs, 58, 11.1–11.33, https://doi.org/10.1175/AMSMONOGRAPHS-D-16-0007.1, http://journals.ametsoc.org/doi/10.1175/AMSMONOGRAPHS-D-16-0007.1, 2017.

McFarquhar, G. M., Finlon, J. A., Stechman, D. M., Wu, W., Jackson, R. C., and Freer, M.: University of Illinois/Oklahoma Optical Array Probe (OAP) Processing Software, https://doi.org/10.5281/zenodo.1285969, https://doi.org/10.5281/zenodo.1285969, 2018.

Mitchell, D. L.: Use of Mass- and Area-Dimensional Power Laws for Determining Precipitation Particle Terminal Velocities, Journal of the Atmospheric Sciences, 53, 1710–1723, https://doi.org/10.1175/1520-0469(1996)053<1710:UOMAAD>2.0.CO;2, 1996.

Mitchell, D. L. and Arnott, W. P.: A Model Predicting the Evolution of Ice Particle Size Spectra and Radiative Properties of Cirrus Clouds. Part II: Dependence of Absorption and Extinction on Ice Crystal Morphology, Journal of the Atmospheric Sciences, 51, 817–832, https://doi.org/10.1175/1520-0469(1994)051<0817:AMPTEO>2.0.CO;2, https://journals.ametsoc.org/doi/abs/10.1175/1520-0469%281994%29051%3C0817%3AAMPTEO%3E2.0.CO%3B2, 1994.

Mitchell, D. L., Zhang, R., and Pitter, R. L.: Mass-Dimensional Relationships for Ice Particles and the Influence of Riming on Snowfall Rates, Journal of Applied Meteorology, 29, 153–163, https://doi.org/10.1175/1520-0450(1990)029<0153:MDRFIP>2.0.CO;2, 1990.

Nakaya, U. and Terada, T. J.: Simultaneous Observations of the Mass, Falling Velocity and Form of Individual Snow Crystals, Journal of the Faculty of Science, Hokkaido Imperial University, 1, 191–200, http://hdl.handle.net/2115/34452, 1935.

Nevzorov, A. N.: Aircraft cloud water content meter, in: Communications a la VIIIeme Conference Internationale sur la Physique des Nuages, pp. 701–703, AIMPA, 1980.

Olson, W. S., Tian, L., Grecu, M., Kuo, K.-S., Johnson, B. T., Heymsfield, A. J., Bansemer, A., Heymsfield, G. M., Wang, J. R., and Meneghini, R.: The Microwave Radiative Properties of Falling Snow Derived from Nonspherical Ice Particle Models. Part II: Initial Testing Using Radar, Radiometer and In Situ Observations, Journal of Applied Meteorology and Climatology, 55, 709–722, https://doi.org/10.1175/JAMC-D-15-0131.1, http://dx.doi.org/10.1175/JAMC-D-15-0131.1, 2016.

Park, S.-G., Bringi, V. N., Chandrasekar, V., Maki, M., and Iwanami, K.: Correction of Radar Reflectivity and Differential Reflectivity for Rain Attenuation at X Band. Part I: Theoretical and Empirical Basis, Journal of Atmospheric and Oceanic Technology, 22, 1621–1632, https://doi.org/10.1175/JTECH1803.1, http://journals.ametsoc.org/doi/abs/10.1175/JTECH1803.1, 2005.

Schmitt, C. G. and Heymsfield, A. J.: The Dimensional Characteristics of Ice Crystal Aggregates from Fractal Geometry, Journal of the Atmospheric Sciences, 67, 1605–1616, https://doi.org/10.1175/2009JAS3187.1, http://dx.doi.org/10.1175/2009JAS3187.1, 2010.

Szyrmer, W. and Zawadzki, I.: Snow Studies. Part II: Average Relationship between Mass of Snowflakes and Their Terminal Fall Velocity, Journal of the Atmospheric Sciences, 67, 3319–3335, https://doi.org/10.1175/2010JAS3390.1, http://journals.ametsoc.org/doi/abs/10.1175/2010JAS3390.1, 2010.

Wang, J., Dong, X., and Xi, B.: Investigation of ice cloud microphysical properties of DCSs using aircraft in situ measurements during MC3E over the ARM SGP site, Journal of Geophysical Research: Atmospheres, 120, 3533–3552, https://doi.org/10.1002/2014JD022795, https://agupubs.onlinelibrary.wiley.com/doi/10.1002/2014JD022795, 2015.

Wu, W. and McFarquhar, G. M.: On the Impacts of Different Definitions of Maximum Dimension for Nonspherical Particles Recorded by 2D Imaging Probes, Journal of Atmospheric and Oceanic Technology, 33, 1057–1072, https://doi.org/10.1175/JTECH-D-15-0177.1, http://dx.doi.org/10.1175/JTECH-D-15-0177.1, 2016.

Xu, Z. and Mace, G. G.: Ice Particle Mass–Dimensional Relationship Retrieval and Uncertainty Evaluation Using the Optimal Estimation Methodology Applied to the MACPEX Data, Journal of Applied Meteorology and Climatology, 56, 767–788, https://doi.org/10.1175/JAMC-D-16-0222.1, http://journals.ametsoc.org/doi/10.1175/JAMC-D-16-0222.1, 2017.

Zhang, P., Zrnić, D., and Ryzhkov, A.: Partial Beam Blockage Correction Using Polarimetric Radar Measurements, Journal of Atmospheric and Oceanic Technology, 30, 861–872, https://doi.org/10.1175/JTECH-D-12-00075.1, http://journals.ametsoc.org/doi/abs/10.1175/JTECH-D-12-00075.1, 2013.

Zikmunda, J. and Vali, G.: Fall Patterns and Fall Velocities of Rimed Ice Crystals, Journal of the Atmospheric Sciences, 29, 1334–1347, https://doi.org/10.1175/1520-0469(1972)029<1334:FPAFVO>2.0.CO;2, 1972.

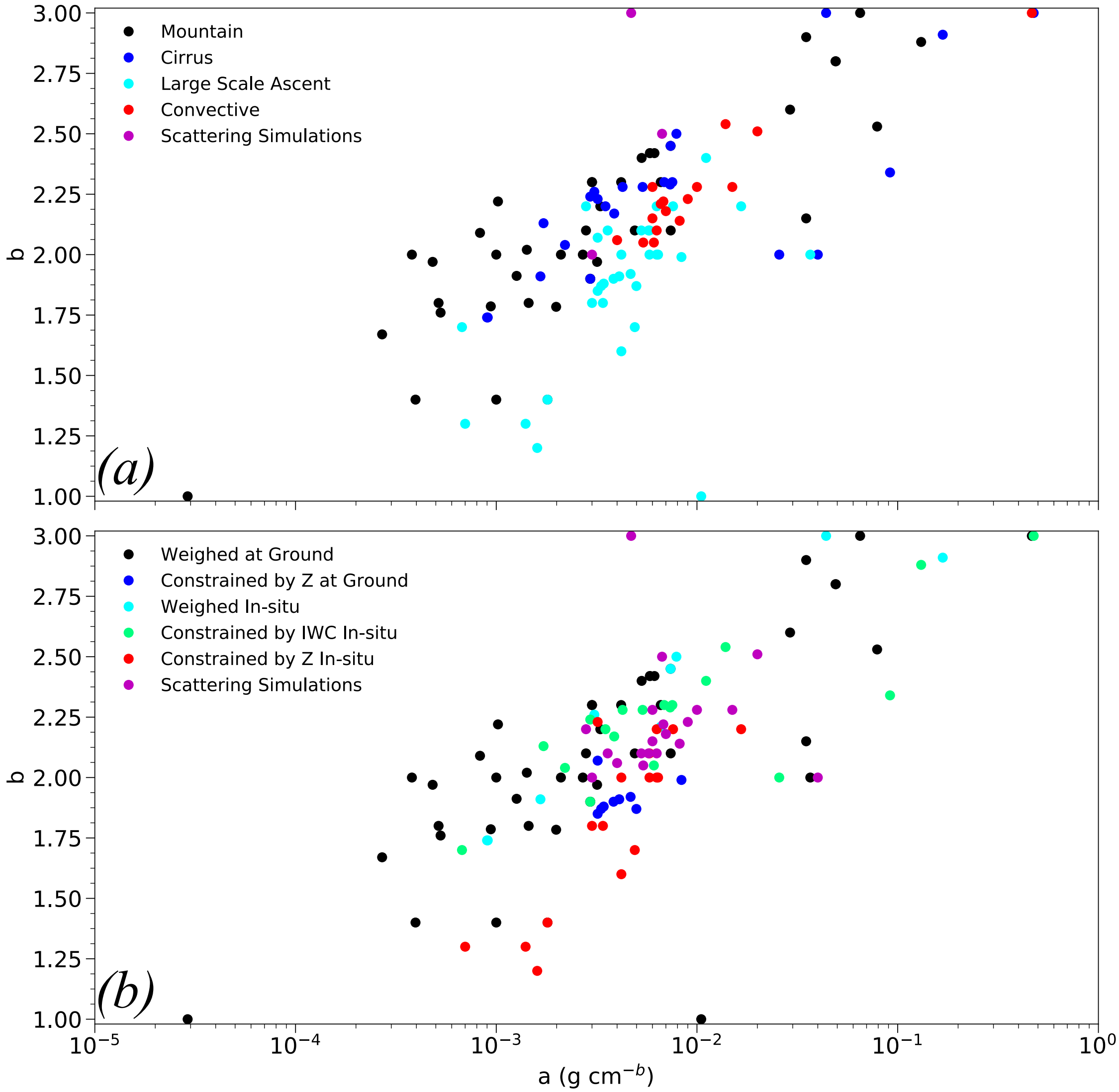

Figure 1. Distribution of a and b coefficients used to characterize $m = aD^b$ relationship from past studies. Points colored by the (a) environment in which measurements were made and (b) technique used to derive the relations.

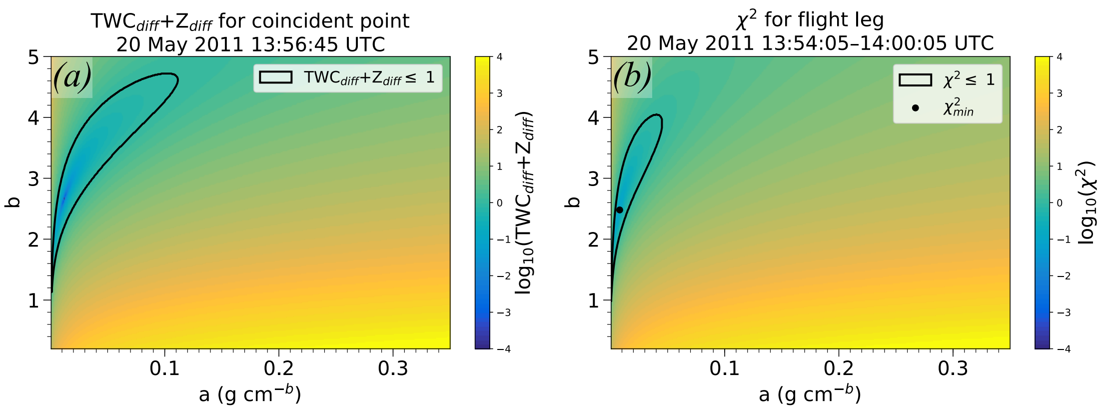

Figure 2. $TWC_{\rm diff} + Z_{\rm diff}$ in (*a*,*b*) phase space for (a) a 10 s coincident point beginning 13:56:15 UTC on 20 May 2011 and (b) integrated over the encompassing flight leg between 13:54:14 and 13:59:35 UTC and normalized by the number of observations N. The black dot in (b) denotes the a and b minimizing χ^2.

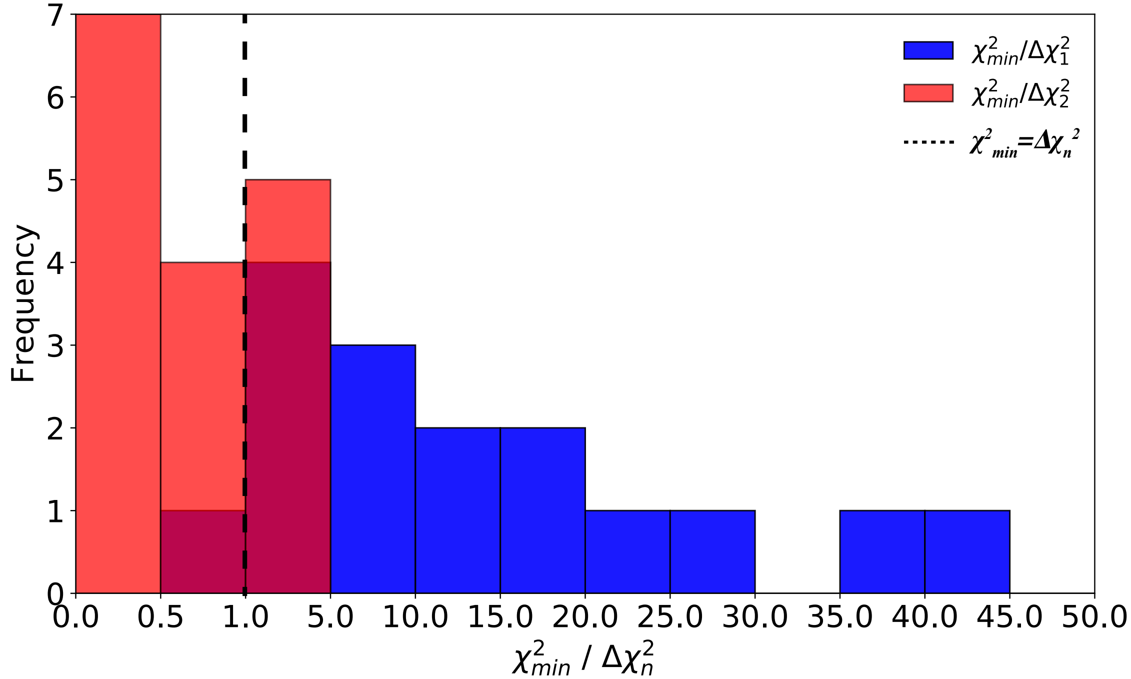

Figure 3. Frequency of $\chi^2_{min}/\Delta\chi^2_1$ (blue shading) and $\chi^2_{min}/\Delta\chi^2_2$ (red shading), where χ^2_{min} ~~and~~ , $\Delta\chi^2_1$, and $\Delta\chi^2_2$ derived for each flight leg used in analysis.

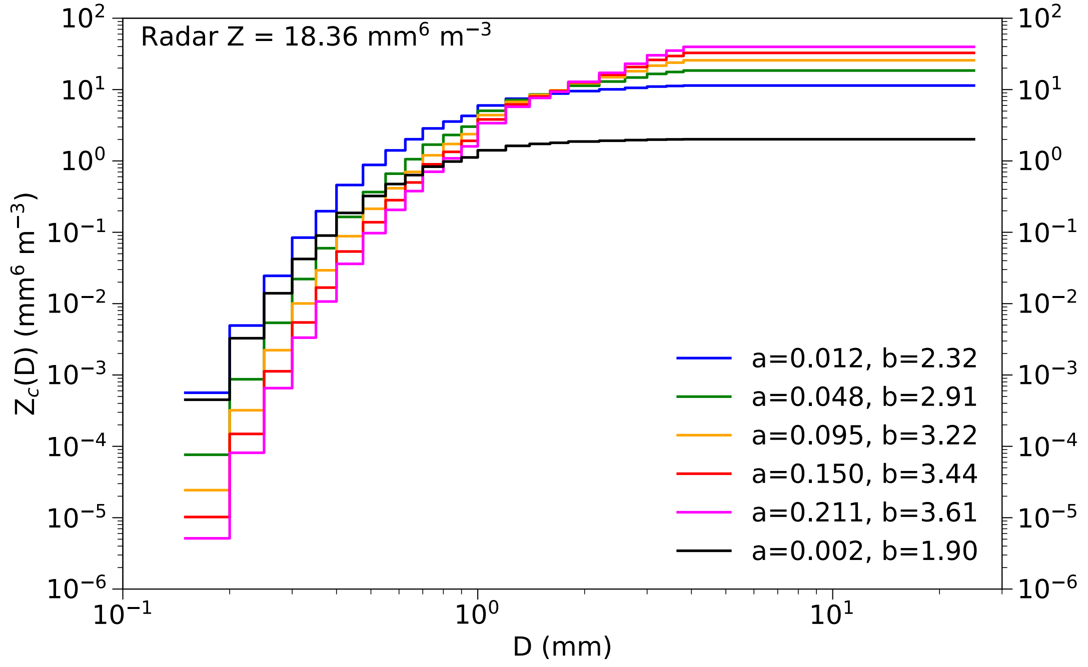

Figure 4. *$Z_c(D)$* as a function of *D* derived using modified *m-D* coefficients from BF95 (black) and from the 5th (blue), 25th (green), 50th (orange), 75th (red), and 95th (magenta) percentiles from the set of equally plausible *m-D* coefficients in order of increasing *b* and *a* values for the 14:16:30–14:32:15 UTC flight leg on 20 May 2011. Mean radar reflectivity matched at the aircraft's position for the same period is listed in top left.

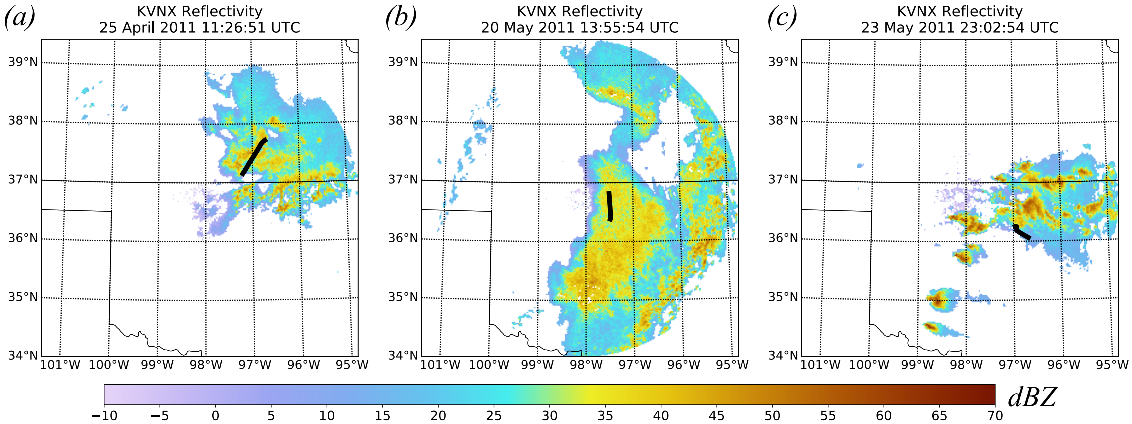

Figure 5. 0.5 degree PPI scan of corrected radar reflectivity from the KVNX radar for (a) 11:26:51 UTC 25 Apr 2011, (b) 14:04:34 UTC 20 May 2011, and (c) 23:02:54 UTC 23 May 2011. Black lines denote the Citation flight track for the constant-temperature leg corresponding to the radar image shown.

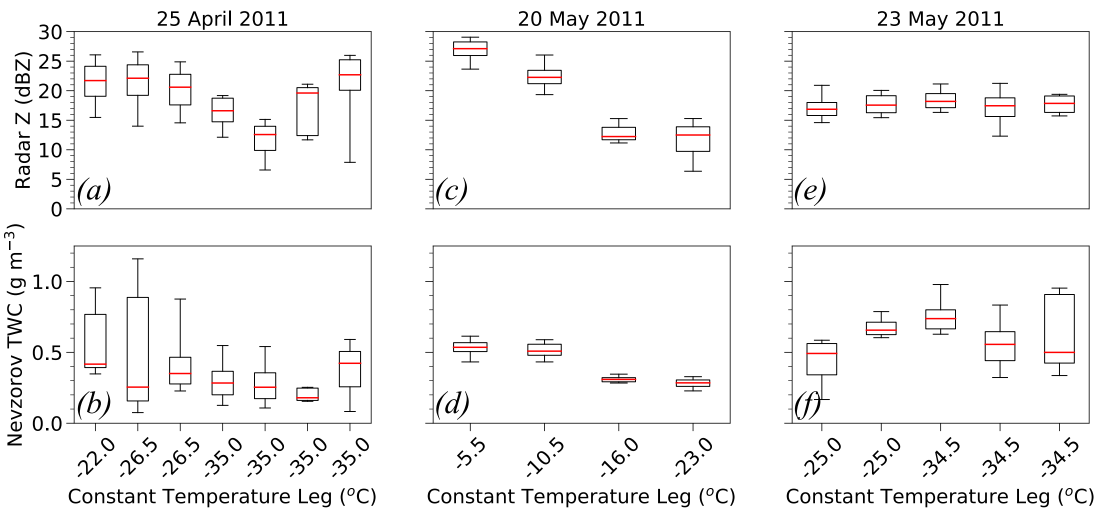

Figure 6. Distribution of matched *Z* (top) and *TWC* from the Nevzorov probe (bottom) for each constant-temperature leg on 25 Apr (left), 20 May (center), and 23 May 2011 (right). Whiskers represent the 5th and 95th percentiles, box edges are the 25th and 75th percentiles, and the line in the middle is the median. Cases where multiple legs of the same temperature exist are shown in chronological order.

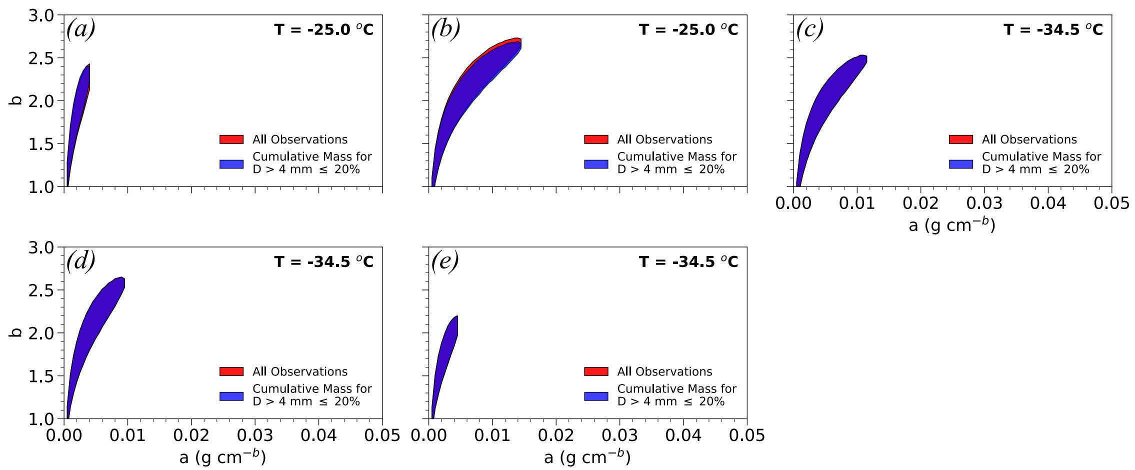

Figure 7. Surfaces of equally plausible a and b values from the $m = aD^b$ relation from each near-constant temperature leg on 23 May 2011 for all coincident observations (red) and only those where cumulative mass for $D > 4$ mm is ≤ 20 % (blue). Flight legs of the same temperature are shown in chronological order.

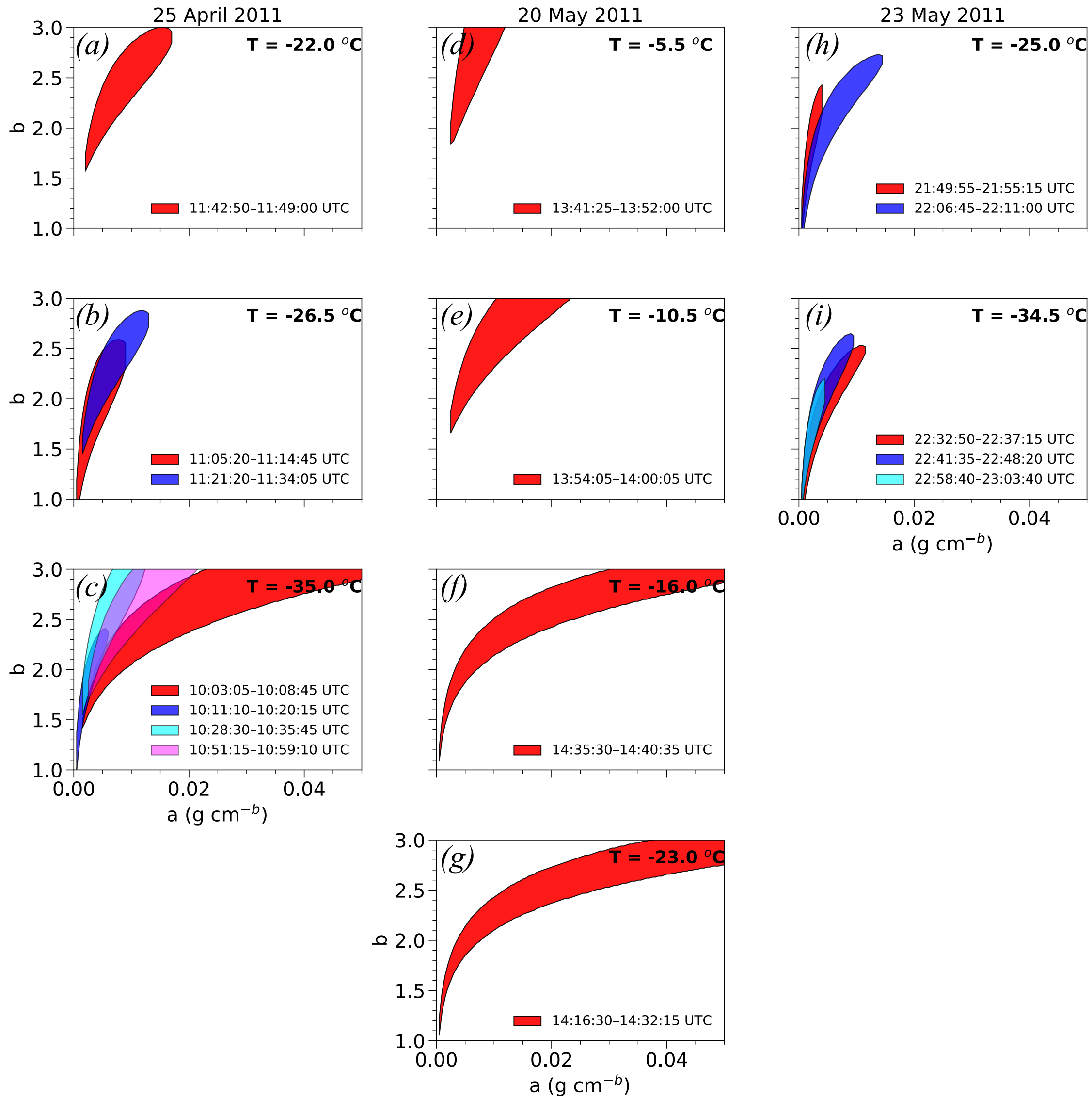

Figure 8. Surfaces of equally plausible *a* and *b* values for near-constant temperature flight legs for the (a–c) 25 April, (d–g) 20 May, and (h–i) 23 May 2011 events. Multiple legs occupying the same temperature are assigned a different color within a panel.

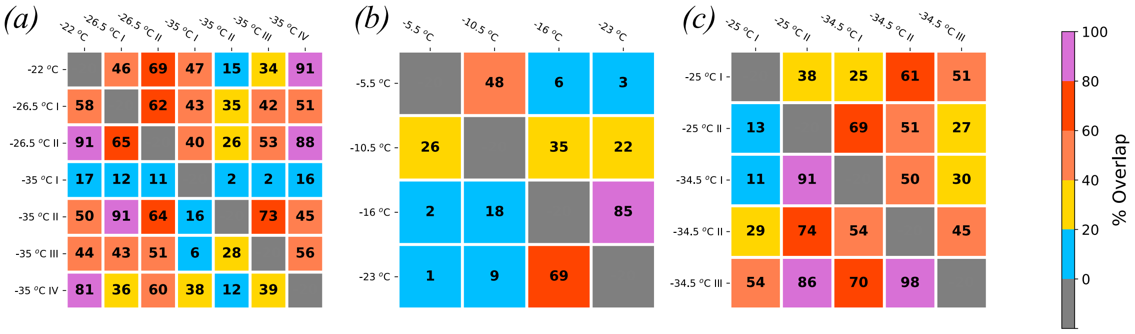

Figure 9. Matrix of overlap area between the equally plausible (*a,b*) surfaces corresponding to each row and column for (a) 25 April, (b) 20 May, and (c) 23 May 2011. The overlap area for each square is normalized by the area of the (*a,b*) surface corresponding to the flight leg listed in each row.

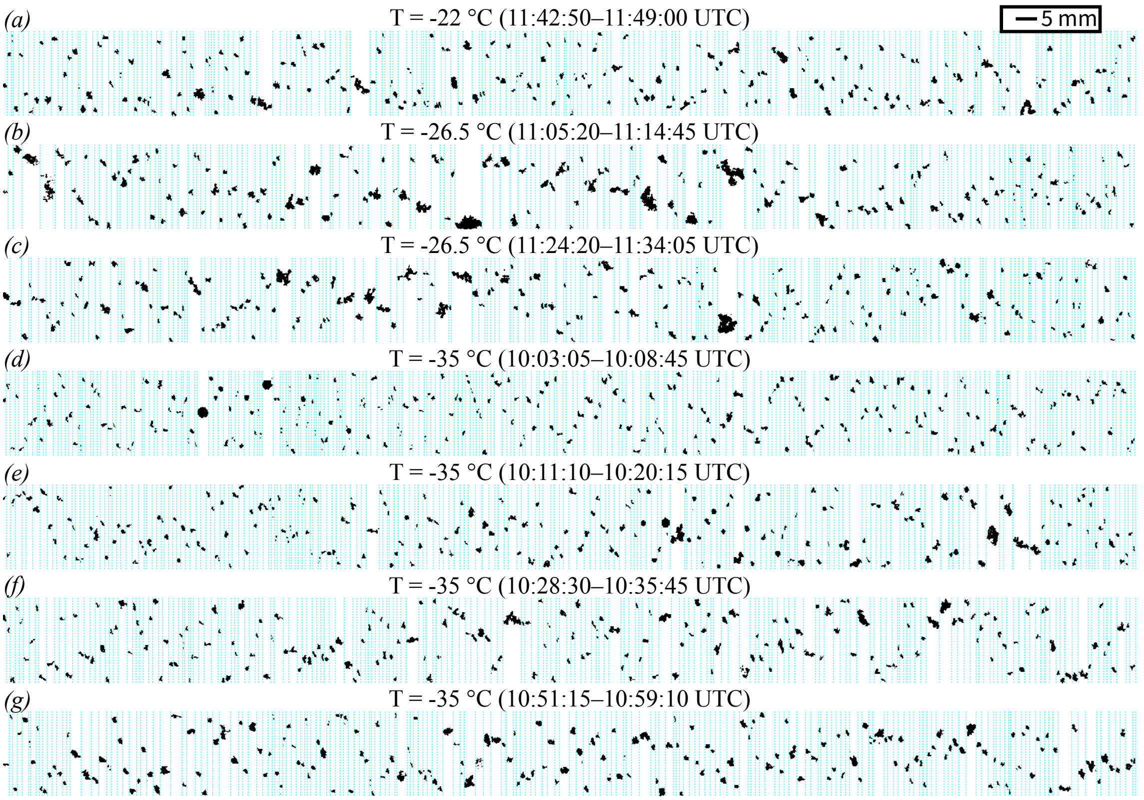

Figure 10. Representative particle images from the HVPS-3 for each near-constant temperature flight leg on 25 April 2011.

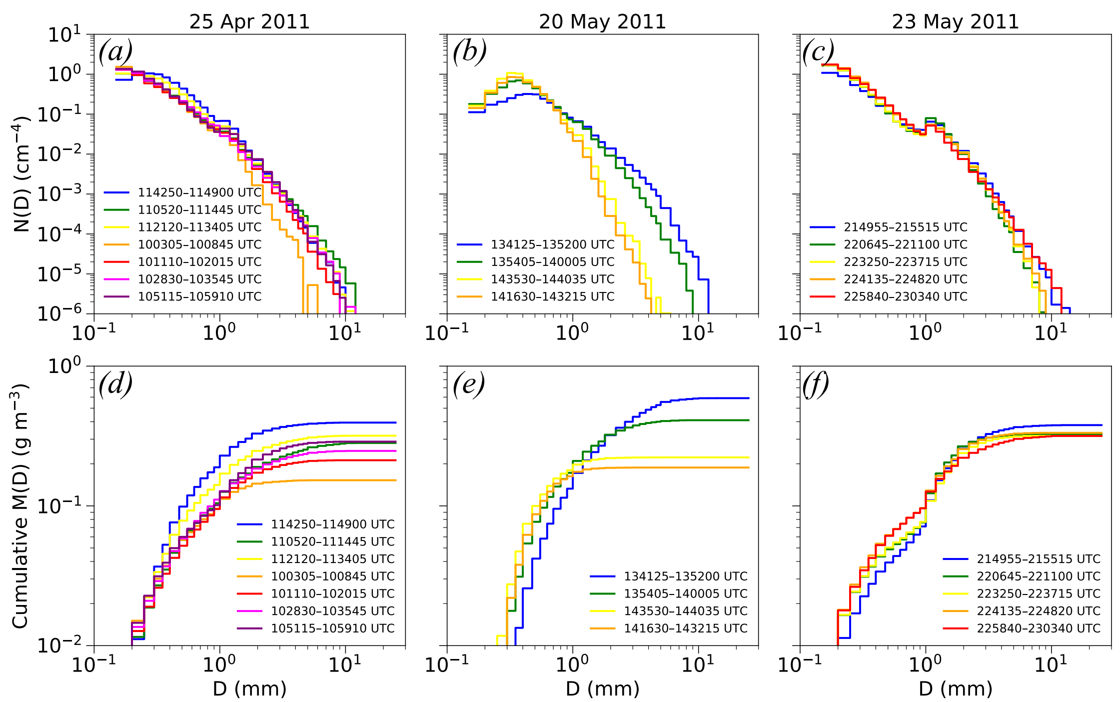

Figure 11. Mean *N(D)* (top) and cumulative *M(D)* (bottom) for each constant-temperature leg on 25 Apr (left), 20 May (center), and 23 May 2011 (right). Cases where multiple legs of the same temperature exist are shown in chronological order.

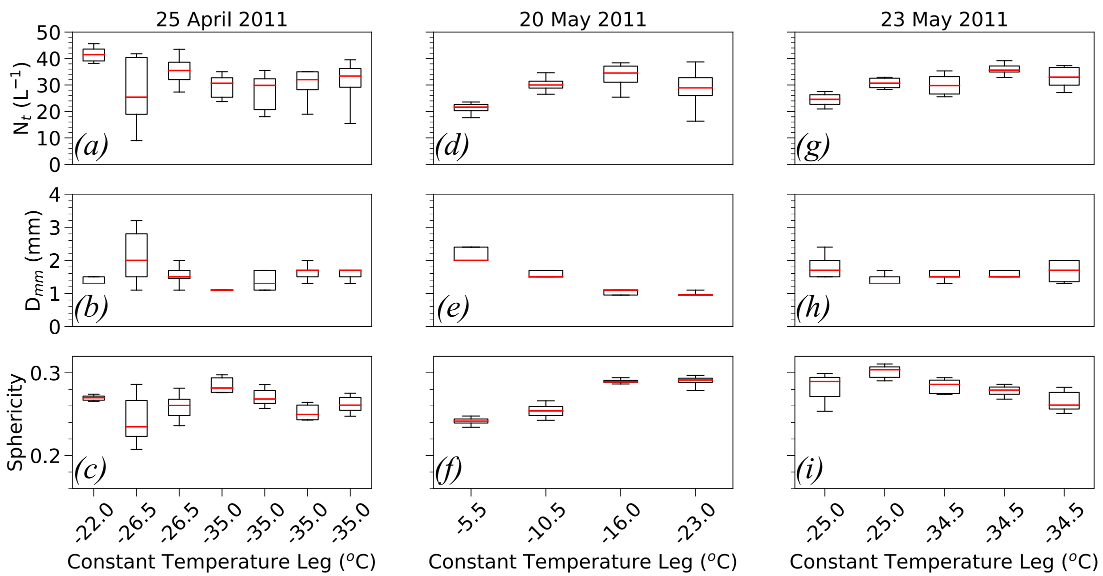

Figure 12. As in Fig. 6, but for number concentration N_t, median mass diameter D_{mm}, and mass-weighted mean sphericity.

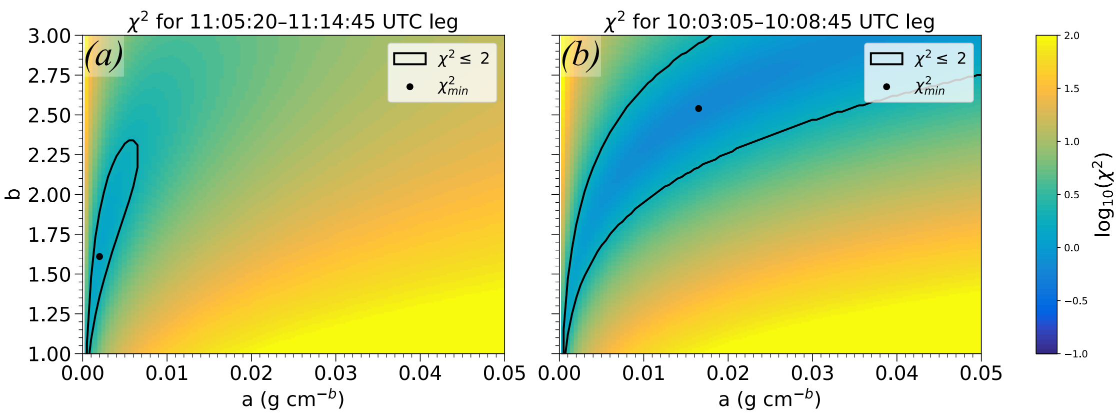

Figure 13. χ^2 statistic in (a,b) phase space for the (a) 11:05:20–11:14:45 UTC and (b) 10:03:05–10:08:45 UTC flight legs on 25 April 2011. Outlined regions represent $\chi^2 \leq 2$ and the dots ${\chi^2}_{\mathrm{min}}$.

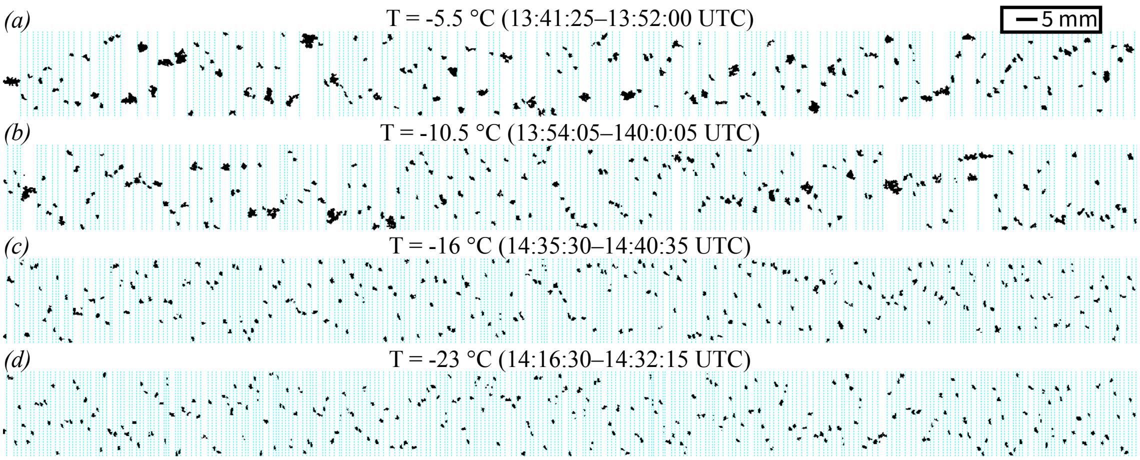

Figure 14. Same as in Fig. 10, but for the 20 May 2011 case.

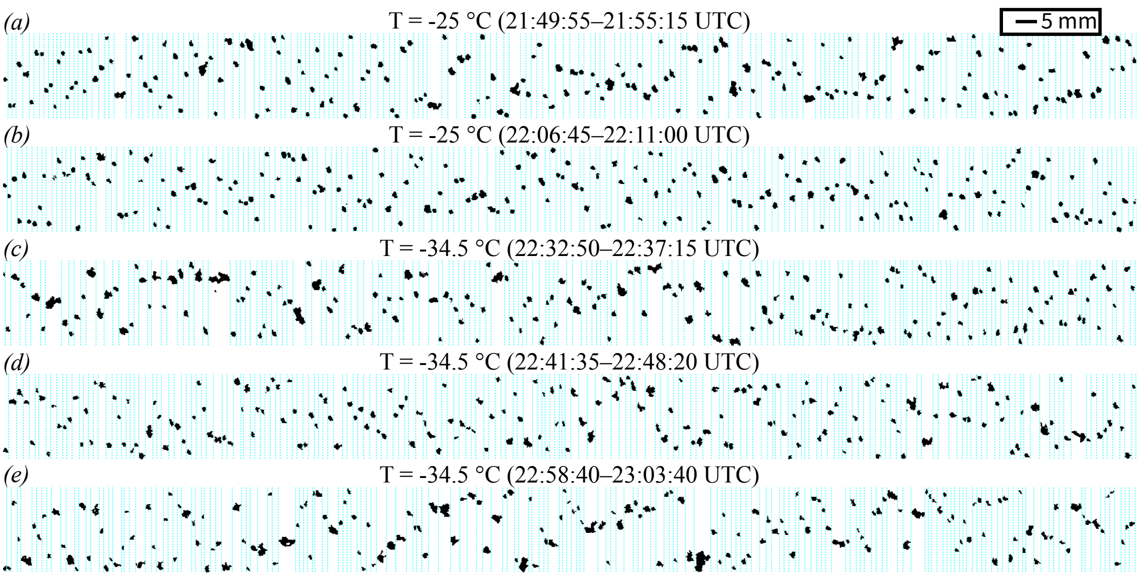

Figure 15. Same as in Fig. 10, but for the 23 May 2011 case.

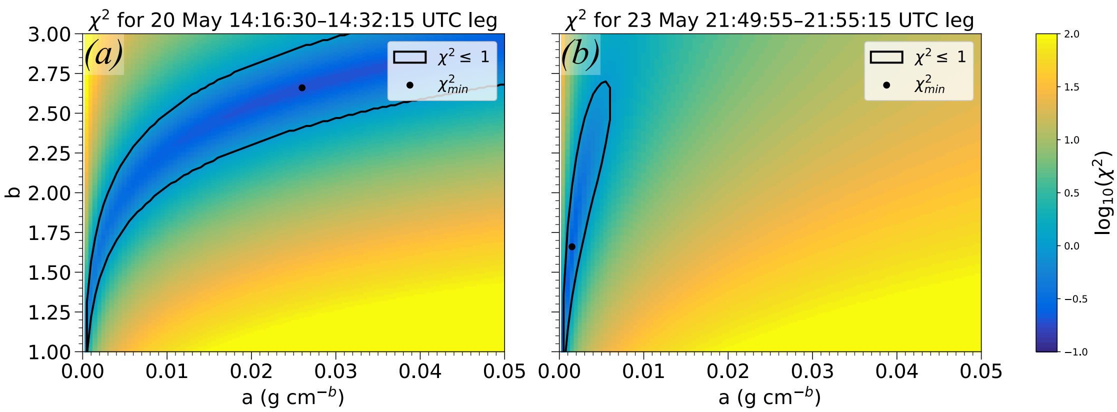

Figure 16. Same as in Fig. 13, but for (a) 14:16:30–14:32:15 UTC on 20 May and (b) 21:49:55–21:55:15 UTC on 23 May 2011. Outlined regions represent $\chi^2 \leq 1$ and the dots $\chi^2{}_{\mathrm{min}}$.

Table 1. List of constant temperature flight legs used in the analysis for which coincident data between the ground-based radar and UND Citation exist. Start and end times, mean altitude, and temperature displayed.

Mean Temp. [°C]	Mean Alt. [km]	Start Time [UTC]	End Time [UTC]
25 April 2011			
-22.0	6.8	11:42:50	11:49:00
-26.5	7.4	11:05:20	11:14:45
-26.5	7.4	11:21:20	11:34:05
-35.5	8.3	10:03:05	10:08:45
-35.5	8.3	10:11:10	10:20:15
-35.5	8.3	10:28:30	10:35:45
-35.5	8.3	10:51:15	10:59:10
20 May 2011			
-5.5	5.0	13:41:25	13:52:00
-10.5	5.9	13:54:05	14:00:05
-16.0	6.9	14:35:30	14:40:35
-23.0	7.9	14:16:30	14:32:15
23 May 2011			
-25.0	7.9	21:49:55	21:55:15
-25.0	7.9	22:06:45	22:11:00
-34.5	9.1	22:32:50	22:37:15
-34.5	9.1	22:41:35	22:48:20
-34.5	9.1	22:58:40	23:03:40

Table 2. List of constant temperature flight legs and the ratio between Z_{diff} and TWC_{diff} valid at the (a,b) that minimize χ^2.

25 April 2011		20 May 2011		23 May 2011	
Times [UTC]	$\frac{Z_{\mathrm{diff}}}{TWC_{\mathrm{diff}}}$	Times [UTC]	$\frac{Z_{\mathrm{diff}}}{TWC_{\mathrm{diff}}}$	Times [UTC]	$\frac{Z_{\mathrm{diff}}}{TWC_{\mathrm{diff}}}$
11:42:50–11:49:00	2.02	13:41:25–13:52:00	4.92	21:49:55–21:55:15	1.52
11:05:20–11:14:45	0.81	13:54:05–14:00:05	6.31	22:06:45–22:11:00	1.82
11:21:20–11:34:05	1.62	14:35:30–14:40:35	3.2	22:32:50–22:37:15	0.99
10:03:05–10:08:45	0.8	14:16:30–14:32:15	3.99	22:41:35–22:48:20	1.82
10:11:10–10:20:15	1.5			22:58:40–23:03:40	0.32
10:28:30–10:35:45	8.58				
10:51:15–10:59:10	1.76				